SURFACE WAVE EFFECTS ON THE UPPER OCEAN RESPONSES TO FAST-MOVING STORMS

by

Qi Wang

Submitted in partial fulfilment of the requirements
for the degree of Master of Science

at

Dalhousie University
Halifax, Nova Scotia
April 2018

Table of Contents

List of Tables

List of Figures

Abstract

Numerical models generally have problems in the prediction of storm intensities due partially to inadequate simulations of the upper ocean mixing and related upper ocean responses to storms. Although ocean waves have been regarded as essential roles in the upper ocean mixing, their effects are not always explicitly incorporated in model simulations. This study is to examine the surface wave effects on upper ocean responses to fast-moving storms based on both observations and numerical simulations. A one-dimensional depth-dependent ocean turbulence model known as GOTM is modified by incorporating surface gravity wave effects including wave breaking, Langmuir circulation and Coriolis-Stokes force. This newly-modified model is applied to simulate the upper ocean responses to Hurricane Arthur (2014) and Hurricane Felix (1995). The model results demonstrate that the incorporation of wave effects, particularly the wave breaking and Langmuir circulation, improves GOTM simulations. Wave effects improve the simulations of the upper ocean thermal responses by significantly enhancing the upper ocean cooling and deepening the simulated mixed layer depth, which leads to better agreement with observations. Wave effects also significantly improve the simulation of near-inertial current amplitudes especially near the base of the ocean mixed layer. With the incorporation of wave effects, the near-inertial energy is transported more efficiently to deeper layers.

List of Abbreviations Used

Abbreviation	Definition
1D	one-dimensional
3D	three-dimensional
AVHRR	Advanced Very High-Resolution Radiometer
BATS	Bermuda Atlantic time-series study
BTM	Bermuda testbed mooring
COARE	coupled ocean-atmosphere response experiment
CC	correlation coefficient
CSF	Coriolis-Stokes force
DIH	depth-integrated heat anomaly
GOTM	General Ocean Turbulent Model
IFREMER	French Research Institute for Exploitation of the Sea
La_t	turbulent Langmuir number
LC	Langmuir circulation
LES	Large-Eddy Simulation
MAE	mean absolute error
ME	mean error
OML	ocean mixed layer
NEMO	Nucleus for European Modelling of the Ocean
NIC	near-inertial current
NODC	National Oceanographic Data Center
OGCM	ocean general circulation models
OTN	ocean tracking network

Abbreviation	Definition
RMSD	root mean square deviation
ROMS	Regional Ocean Modelling System
RUWRF	Rutger University Weather Research and Forecasting model
SLP	air pressure at the sea level
SST	sea surface temperature
TKE	turbulent kinetic energy
UTC	coordinated universal time
WB	wave breaking
WW3	WAVEWATCHIII

Acknowledgements

It is my great pleasure to acknowledge a large number of people who gave me great help during my thesis work.

I would first like to sincerely thank my supervisor, Dr. William Perrie, for his guidance, patience, inspiration, and for being supportive throughout. The door of his office was always open for me when I had troubles no matter in my research or in my life. I am sincerely grateful for the numerous hours he spent on revising my writings, helping me with presentation practicing, and organizing discussions and ISMC events which lent me a hand to get used to the foreign language and the different culture. I thank him for encouraging me and providing financial support to attend conferences and workshops to build my confidence in giving public presentations.

I would also like to thank my supervisor, Dr. Jinyu Sheng, for his wonderful course teaching of numerical modelling and coastal dynamics, which opened the door to numerical modelling well. He not only helped me with my studies but also brought a sense of belonging to all the Chinese students, especially during traditional Chinese festivals.

I am also grateful to other members of my advisory committee, Dr. Stephanie Kienast and Dr. Bechara Toulany, who contributed helpful guidance and comments in my MSc studies. Their profound suggestions and careful revision gave me great help in improving my writing and presenting skills. I would also like to thank Dr. David Greenberg for being my external examiner, taking time to read my thesis and proposing thoughtful comments.

A very special gratitude goes out to Dr. Guoqiang Liu for his inspiring scientific ideas and for countless hours on my research discussions. Many people have helped me in my course studies. I sincerely thank Dr. Daniel Kelley and Dr. Douglas Wallace, who showed the attractiveness of physical and chemical oceanography. I would also like to express my thanks to fellow students, to the staff and the Faculty of the Department of Oceanography and the Bedford Institute of Oceanography and acknowledge the financial support from the MEOPAR. Thank you also to the SEADOG Intramural climbing team and DalDance Society for helping me to get rid of the winter blues.

Finally, I must express my very profound gratitude to my husband Rui Zhang for his unfailing and dependable support and companionship. I am also grateful to my other family members and friends who have supported me along the way.

Chapter 1
Introduction

1.1 Background

Hurricanes are among the most destructive natural hazards. Reliable predictions of hurricane tracks and intensities can help reduce unnecessary human life losses and property damages, and thus there are significant ongoing efforts to improve all aspects of hurricane forecasting. One of essential factors is to understand the ocean response to the hurricane forcing. Typically, the passage of a storm represents one of the most extreme air-sea interactions, accompanying vigorous ocean responses [e.g., Emanuel 1991], including both the thermal response such as sea surface temperature (SST) cooling and the dynamic response such as the generation of strong near-inertial currents [e.g., Ginis 1995; Ginis 2002]. Subsequently, these ocean responses can in turn feed back to the dynamics of the hurricane system. Previous studies [Perlroth, 1969; Leipper and Volgenau, 1972] pointed out the importance of subsurface stratification determined by the upper ocean thermal structure and the advection by currents on the storm intensity. The significance of SST cooling has also been shown to dramatically alter air-sea fluxes within the high-wind storm systems and thus modify the intensities of hurricane systems [Cione et al., 2003]. Glenn et al. [2016] simulated Hurricane Irene with Weather Research and Forecasting (WRF) model using fixed warm pre-storm and cold post-storm

SST boundary conditions given by satellite remote-sensing data. The simulated minimum sea level pressure (SLP) at landfall is reduced by 7-8 hPa in the case of the cold SST boundary, with the maximum wind speed reduced by > 5 m/s. Schade and Emanuel [1999] defined a quantitative measure of SST feedback factor and suggested the SST feedback effect can reduce the hurricane's intensity by more than 50% in the atmosphere-ocean coupled model.

Over last few decades, the accuracy in predicting hurricane trajectories has been improved; while there has been little improvement in the skill in predicting the hurricane intensities. During the hurricane passage, there are several major features of ocean responses that are important to predictability: the remarkable upper ocean cooling [e.g. Shay et al., 1992], and notable near-inertial motions [e.g. Leaman and Sanford, 1975; Dickey et al., 1998; Zedler et al, 2002]. Better knowledge of these ocean responses leads to more accurate simulations and predictions of ocean processes associated with hurricanes. Therefore, the ocean response to hurricanes is an important area of research to further our understanding of air-sea interactions and thus to improve model predictions of both storm tracks and intensities. However, measurements available for such studies are very sparse because of the difficulty of routine shipboard observations under hurricane adverse conditions and consequently these measurements are scarce. So far, most of the observational studies of ocean responses to storms are based on satellite remote sensing data or very limited *in situ* data, such as Argo floats, airborne expendable Bathy Thermographs, Electromagnetic Autonomous Profiling Explorers (EM-APEX) [e.g., D'Asaro 2003; Sanford et al., 2011], and especially the moored measurements which are

widely used for comparative numerical studies [e.g., Dickey et al., 1998, 2001; Zedler et al., 2002]. However, vertical resolutions of moored measurements were often too coarse to fully resolve the upper oceanic vertical structure [e.g., Brainerd and Gregg, 1995]. Recently, underwater gliders were found to be useful in making high resolution measurements under intense wind forcing [e.g., Ruiz et al., 2012; Domingues et al., 2015].

For numerical studies, three-dimensional (3D) ocean models have widely been used to examine the upper ocean response to hurricanes [e.g. Sheng et al., 2006; Oey et al., 2007; Yablonsky and Ginis, 2009]. The shear-induced turbulent mixing in the upper ocean, accompanied by the entrainment of cooler thermocline water, is the primary mechanism for the SST cooling during the storm passage [Price, 1981; Black, 1983; Bender et al., 1993]. To emphasize the study of 1D shear-induced mixing processes and the surface wave effects which are also 1D-related dynamics, 1D models have been used to investigate the upper ocean responses [e.g., Price et al., 1986; Large et al., 1994; Zedler et al., 2002]. However, the turbulence parameterizations used in many ocean circulation models do not explicitly include effects of surface waves, which have been found to play essential roles in the upper-ocean mixing [e.g., McWilliams et al., 1997; Li et al., 2005; D'Asaro 2014]. The improvements in model simulations thus can be expected with the inclusion of wave-related processes [e.g., Reichl et al., 2016]. In numerical simulations made by ocean general circulation models (OGCM), the ocean mixed layer depth (OML) is usually underestimated [e.g., Qiao et al., 2004]. This can be partly explained by the neglect of surface waves which contribute to the enhancement of upper ocean turbulence

[Agrawal et al., 1992; Huang et al., 2011]. However, due to the lack of observations during passages of storms, there is little chance to assess the model results and examine the wave effects based on the *in situ* measurements, especially under extreme forcing conditions.

1.2 Literature Review

1.2.1 Ocean Responses to Storms

Ginis [1995] suggested that a potentially significant constraint on predictions of storms, especially their intensities, results from the lack of knowledge of the ocean response to extreme wind forcing. Both positive and negative feedbacks are believed to exist in the ocean-storm system. At the stages of genesis and development, since the increasing wind speeds at the sea surface enhance the evaporation rate, the latent heat energy supplied by the enhancement of moisture from the ocean is increased and drives the circulation of the storm [Ooyama, 1969]. This process creates a positive feedback (heat fluxed from ocean to the air) in the storm-ocean system. With the continuous development of the storm, the wind forcing enhances the turbulent level of the upper ocean which induces increased vertical mixing and cooler water entrainment from the thermocline into the overlying mixed layer, thus decreasing the upper ocean temperature associated with the mixed layer deepening. These processes reduce the total heat flux from the ocean to the storm system, which leads to a negative feedback and modulation of the storm intensity.

During the storm passage, there are several dominant features of ocean responses [e.g. Leaman and Sanford, 1975; Price, 1981; Price, 1983; Gill 1984; Shay et al., 1992; Price et al., 1994; Dickey et al., 1998; Zedler et al, 2002; Sheng et al., 2006; Wang and Sheng, 2016; Xie et al., 2008; Lemay et al., 2018], including the remarkable upper ocean cooling, generation of sheared near-inertial currents, horizontal and vertical propagation of near-inertial internal waves, storm surge and the impacts on carbon cycling in coastal areas. Good knowledge of these ocean responses to storms will be very useful to have more realistic storm simulations and predictions.

Numerous studies have been made on the examination of ocean responses to hurricanes based on both observations [e.g. Black, 1983; Lai and Sanford, 1986] and theoretical and numerical models [e.g. Price, 1981, 1983; Gill, 1984; Chang, 1985; Sheng et al., 2006], which highlight two major ocean responses, i.e. the upper ocean cooling and the generation of strong inertial motions.

In early studies, the SST cooling was documented to reach several Celsius degrees after the passage of storms [Fisher 1958], with the maximum SST cooling occurring in the right-rear quadrant of the wind field, often as a function of storm intensity [Jordan 1964; Wright 1969; Black 1983]. Shay et al. (1992) investigated the upper ocean response to the passage of Hurricane Gilbert (1988) using *in situ* observations. They found a significant SST drop of 3.5-4 °C and the maximum currents in the mixed layer ranging from 1 to 1.4 ms^{-1}. Observations of ocean currents generated by storms are much sparser than those of temperature [Ginis, 1995; Shay, 2010]. Most of the available observations were from buoys and mooring data which only measure currents at certain

depths with relatively coarse spatial resolution. Shay et al. [1992] described the 3-D upper-ocean current response to Hurricane Gilbert and presented the significant rightward asymmetry feature. The current velocities reached the magnitude of >1 m/s in the mixed layer and presented considerable velocity shear near the base of the OML. The associated near-inertial flows usually are a slightly frequency shifted above the local inertial period by 1-20%, which depends on storm characteristics and the ocean stratification.

Previous numerical studies [e.g. Price 1981; Black 1983; Bender et al. 1993; Sheng et al, 2006; Wang and Sheng, 2016] have indicated that the major mechanism for the upper ocean cooling is the turbulent mixing during the passage of storms. The heat fluxes, such as surface sensible and latent heat fluxes to the atmosphere, usually play minor roles, only accounting for less than 20% of the total SST decrease [Ginis 1995; Price 1981; Emanuel 2001; Trenberth and Fasullo, 2007]. The 3D processes, such as transient upwelling [Price 1981; Emanuel 2001], horizontal advection of warm water away from the storm center [Leipper 1967], also play roles, especially for the slowly moving storm and the relaxation stage [Yablonsky and Ginis 2009]. Sheng et al. [2006] conducted two model experiments with and without advection terms under an idealized relatively rapidly-moving storm. They suggested that vertical mixing plays a dominant role in the SST cooling since most of the SST cooling is captured by the case without advection. Zedler et al. [2002] explored the ocean response to Hurricane Felix (1995) with the Bermuda Testbed Mooring (hereafter BTM) data and simulated the ocean response with four different 1D mixed layer models. They concluded that 1D models can partly simulate the oceanic responses for both temperature and currents, though without the

inclusion of 3D processes, e.g. horizontal advection, Ekman pumping induced upwelling and the propagation of internal waves. Therefore, the important contribution of 1D vertical mixing processes has been highlighted. Some studies have suggested improving simulations of the storm-induced SST cooling by coupling a 1D ocean model to a hurricane model [e.g. Emanuel et al., 2004; Lin et al. 2005, 2008; Bender et al. 2007]. However, there are few studies that include the wave effects in their simulations of the upper ocean responses to storms, though the surface gravity wave effects have been proven to be important in the upper ocean mixing [e.g. D'Asaro, 2014] as we will describe in detail in the next part.

1.2.2 Surface Wave Effects on the Upper Ocean Mixing

In general, surface waves affect the upper ocean turbulence mainly through processes of surface wave breaking (hereafter WB), the Coriolis-Stokes force (CSF), and Langmuir circulation (LC) [e.g., D'Asaro, 2014]. The combined effects of these wave-induced mixing mechanisms can further influence the oceanic boundary layer turbulence (Sullivan and McWilliams, 2010), submesoscale processes including surface fronts and filaments (Hamlington et al., 2014), and global climate simulations (Fan and Griffies, 2014; Li et al., 2016).

Laboratory measurements [Rapp and Melville, 1990; Melville et al., 2002] and the model simulations [Sullivan et al., 2007] demonstrate that surface wave breaking could induce remarkable losses of both energy and momentum from the wave field. The lost energy is transferred from waves to turbulences [e.g. Agrawal et al., 1992], enhances the

level of turbulence, and contributes to mixing [e.g., D'Asaro 2014]; the lost momentum is considered to be transferred from the wave field to the underlying current field, and modifies the vertical profiles of mean horizontal currents [Sullivan et al., 2004; 2007]. Note that effects of WB are usually confined within the upper-most layer with thickness comparable to the significant wave heights. In the turbulence-resolving models, the high temporal and spatial resolutions allow models to capture the characteristic scales of turbulence directly. Noh et al. [2004] used a 3D Large-Eddy Simulation (LES) model to investigate the effect of wave breaking on the Ocean Boundary Layer (OBL) by imposing an additional random force at the sea surface to imitate the WB-induced turbulent kinetic energy (TKE) injection. Since this method excludes the dynamics of breakers, Sullivan et al. [2004, 2007] implemented the WB terms in a direct numerical simulation, as 3D parameterized, time-dependent, randomly surface distributed breakers, and concluded that WB contributed to both the TKE flux and the momentum flux. In large-scale ocean general circulation models where the turbulent scale processes are parameterized, the vertical turbulent schemes usually do not incorporate surface wave effects explicitly. Craig and Banner [1994] first parameterized the WB-induced energy flux as a source of TKE injection to turbulence at the surface in their calculation. With this additional inclusion to a conventional second-order turbulent scheme [e.g. Mellor and Yamada, 1982], a turbulent wave boundary layer, similar to the observations, was successfully reproduced. This approach increases the turbulence levels in the shallow mixed layer, thereby increasing its depth and decreases the associated gradients [Noh and Kim, 1999; Gerbi et al. 2008], both of which lead to better agreement with observations. Based on a

similar idea, Kantha and Clayson [2004] also related the parameterization of the TKE flux to the wind stress in their model. Paskybi et al. [2012] established a method to calculate the TKE with the wave-energy dissipation spectrum. Besides the TKE contribution of the WB effect, He and Chen [2011] established the vertical distribution of the wave breaking stress (momentum flux induced by WB), following the same idea of the stochastic breakers concept employed by Sullivan et al. [2007], and modified the momentum equations of GOTM for the inclusion of this wave breaking stress. These efforts further improved the performance of numerical models in comparison with the observations [He and Chen, 2011]. Here, we propose to use the approaches of Craig and Banner [1994] and He and Chen [2011] to account for contributions of WB to both the energy field and the momentum field.

Stokes drift, a residual flow induced by unclosed wave orbits with greater speed below-crest and smaller speed below-trough, is another important wave-related feature that can influence the upper ocean dynamics, whose influence can be boiled down to two processes. *One* process consists of the interaction with the planetary vorticity [Hasselmann, 1970], called the Coriolis-Stokes force (hereafter CSF) which works as a body force on the mean flow. The effect of CSF has been found to be one of important mechanisms in controlling the dynamics of the upper ocean, i.e. modifying mean-current profiles and thus possibly the temperature structure [Polton et al., 2005].

The second process is the Langmuir circulation (hereafter LC), generated by the interaction between the strong vertical sheared Stokes drift and vertical vorticity [Craik and Leibovich, 1976; Teixeira and Belcher, 2002]. It has long been shown to be a

remarkable contribution to the mixing throughout the mixed layer and thus suggested to be a key mechanism in deepening the mixed layer [e.g., Li et al., 1995; Li and Garrett, 1997; Kukulka et al., 2010; Sullivan and McWilliams, 2010; Belcher et al., 2012; D'Asaro et al., 2014]. Following the theory by Craik and Leibovich [1976], Skyllingstad and Denbo [1995] first reproduced LC in a LES model by adding a vortex force and an additional Stokes drift advection term in the momentum equation, and concluded that LC is important in the structure of the upper ocean by enhancing the vertical velocity and increasing the entrainment heat flux. McWilliams et al. [1997] improved the previous results for LES simulations by accounting for the effect of Stokes drift on the Coriolis and pressure terms and furthermore suggested the LC-induced changes in both the mean-flow and the turbulence fields. Due to these substantial contributions to the vertical mixing in the upper ocean by LC, an important issue appears to be how to properly parameterize the LC effect in OGCMs. Parameterization of LC effects is carried out in terms of modifications of the mixing length scale as well as the inclusion of contributions from the Stokes force in momentum and TKE equations. Kantha et al. [2004] included the LC effect by adding additional Stokes drift induced shear production terms, and simulated magnitudes of associated increases in the TKE and its dissipation rate (induced by the LC effect) very similar to those of LES model results [McWilliams et al. 1997] under same forcing conditions. Following a similar approach, Wu et al. [2015] employed a 1D GOTM model with a k-ϵ scheme at Station Papa to examine surface wave effects based on observational and numerical results. In their study, the LC contribution to the upper ocean mixing, especially under high-wind conditions, was further highlighted. In

this study, we choose a similar parameterization to examine the LC effect on the upper ocean response to extreme wind forcing.

The non-breaking wave induced turbulence, which refers to the turbulence generated by the wave orbital motion directly, has been demonstrated in theoretical analyses, laboratory experiments, and numerical simulations (e.g. Qiao et al., 2004; Babanin, 2006; Pleskachevsky et al., 2011). However, D'Asaro [2014] suggested that the widespread acceptance of the non-breaking wave effect and its parameterization methods have not yet been achieved. Furthermore, Aijaz et al. [2017] acknowledged that the parameterization of turbulence induced by non-breaking waves may have included the contribution of Langmuir circulation implicitly. Thus, subsequently, the portion contributed by the effect of non-breaking waves is still open to discussion. Therefore, in this study we do not incorporate the non-breaking wave effects in this proposed work.

1.3 Objectives

A good knowledge of ocean responses to storms is important in improving the accuracy of model predictions of storms, especially for the intensities. The primary objective of my thesis is thus to examine surface gravity wave effects on the upper ocean response under moving storms, particularly on the processes of vertical mixing, based on both observations and numerical model simulations. The following scientific questions are to be addressed.

(1) Which of the above mentioned surface wave related processes dominate the upper ocean responses to moving storms both over the coastal shelf area and over the open ocean of the Northwest Atlantic?

(2) How do surface gravity waves-related processes impact the upper ocean mixing and thus the upper ocean thermal response to storms?

(3) How do surface gravity waves impact the dynamic response of the upper ocean, e.g. storm-induced near-inertial currents?

In this study, the 1D GOTM with k-ϵ turbulent scheme is applied. The GOTM (version 4.1.0) is modified by adding surface gravity wave related processes, including wave breaking (WB), Coriolis-Stokes force (CSF) and Langmuir circulation (LC). The newly-modified GOTM is employed to the simulations of upper ocean responses to Hurricane Arthur (2014) over the costal ocean and Hurricane Felix (1995) over the open ocean. The high-resolution underwater glider measurements during the passage of Hurricane Arthur and the Bermuda Testbed Mooring measurements during the passage of Hurricane Felix give us valuable opportunities to assess the model simulations and investigate surface wave effects on upper ocean responses to fast-moving hurricanes.

1.4 Structure of Thesis

Chapter 2 describes basic governing equations of GOTM and modifications of incorporating surface wave effects. Chapter 3 describes the application of newly-modified GOTM to Hurricane Arthur (2014) case. This chapter includes the model setup, e.g., description of forcing conditions, initial conditions and experimental design;

overview of meteorological and oceanographic conditions before, during, and after Hurricane Arthur; and the simulations of thermal and dynamic responses of the upper ocean. Chapter 4 presents the model simulation of Hurricane Felix (1995) case over the open ocean with the similar structure to Chapter 3. The final chapter provides a summary and discussion.

Chapter 2

Depth-dependent Ocean Circulation Model

2.1 Overview of GOTM Model

GOTM (General Ocean Turbulence Model) is a one-dimensional depth-dependent model for studying hydrodynamic and thermodynamic processes related to vertical mixing in the ocean. The lateral gradients and advection terms are either neglected or prescribed. GOTM allows for a choice among popular turbulence schemes for the parameterization of vertical turbulent fluxes of momentum, heat, and dissolved and particulate matter [Burchard et al., 1999]. Based on Reynolds decomposition, any turbulent flows can be decomposed into mean and fluctuating components. Thus, GOTM is governed by both mean flow equations and a turbulence model. The 1D mean flows are governed by,

$$\frac{\partial u}{\partial t} = \frac{\partial}{\partial z}\left((\mu_t + \mu)\frac{\partial u}{\partial z}\right) + fv \qquad (2\text{-}1)$$

$$\frac{\partial v}{\partial t} = \frac{\partial}{\partial z}\left((\mu_t + \mu)\frac{\partial v}{\partial z}\right) - fu \qquad (2\text{-}2)$$

where (u, v) are the current velocities in the eastward and northward directions respectively, μ_t is the vertical eddy viscosity, μ is the kinematic viscosity which is much smaller than μ_t and thus can be neglected, g is the gravitational acceleration, f is the Coriolis parameter. Horizontal eddy diffusion parameterizations are not considered here,

because only the effect of vertical means is considered in the one-dimensional form of equations. The advection terms are also neglected in GOTM.

For the turbulent portion, the *k*-ϵ turbulence scheme is used in this study. This scheme is one of the widely-used turbulence parameterizations in the vertical direction, employing equations for k and ϵ. Here k represents the turbulent kinetic energy (TKE) and ϵ represents the dissipation rate. The 1D transport equation for k is expressed as

$$\frac{\partial k}{\partial t} = \frac{\partial}{\partial z}\left(\frac{\mu_t}{\sigma_k}\frac{\partial k}{\partial z}\right) + P + B - \epsilon \qquad (2\text{-}3)$$

where σ_k is the constant Schmidt number for k, B is the buoyancy production, and P is the shear production estimated as

$$P_s = \mu_t\left[\left(\frac{\partial u}{\partial z}\right)^2 + \left(\frac{\partial v}{\partial z}\right)^2\right] \qquad (2\text{-}4).$$

The 1D depth-dependent transport equation of ϵ is expressed as

$$\frac{\partial \epsilon}{\partial t} = \frac{\partial}{\partial z}\left(\frac{\mu_t}{\sigma_\epsilon}\frac{\partial \epsilon}{\partial z}\right) + \frac{\epsilon}{k}(c_{\epsilon 1}P + c_{\epsilon 3}B - c_{\epsilon 2}\epsilon) \qquad (2\text{-}5)$$

where σ_ϵ is the constant Schmidt number for ϵ, and $c_{\epsilon 1}$, $c_{\epsilon 2}$, and $c_{\epsilon 3}$ are empirical coefficients. For specific values, see Rodi [1987], Burchard and Baumert [1995], and Burchard et al. [1998]. The eddy viscosity is parameterized as

$$\mu_t = c_\mu \sqrt{k} l \qquad (2\text{-}6)$$

where c_μ is the stability function and l is the typical turbulent length scale.

2.2 GOTM Modification

The 1D GOTM is used in this study, with modifications of additional surface gravity wave-related processes: surface wave breaking (WB), Coriolis-Stokes force (CSF) and Langmuir circulation (LC). One of widely used turbulence schemes, known as the k-ϵ scheme is employed in this study. The surface wave breaking effects are parameterized as a source of turbulent kinetic energy (TKE) at the sea surface [Craig and Banner, 1994] and a body force representing the momentum flux from wave fields to ocean current fields [He and Chen, 2011]. The CSF is expressed as a force of the interactions between the planetary vorticity and the Stokes drift on the Eulerian momentum balance [Hasselmann, 1970]. The LC effect is parameterized as shear production of Stokes drift [Ardhuin and Jenkins, 2006]. The effect of wave age is also incorporated in the parameterization of wave-related processes. In previous studies [e.g., Craig and Banner, 1994], some of parameterization coefficients are treated as constant values. For instance, in the parameterization of the surface wave breaking induced TKE flux at the sea surface, the wave energy factor is usually set to be constant 100 [Craig and Banner, 1994]. This setting is based on the assumption of fully-developed sea state. However, in our cases, waves under the extreme storm forcing, especially at the early forced stage, are routinely young. Thus, the effects of wave age are also considered in this study. The next section provides the information on the modification of the GOTM model with the surface gravity wave effects.

2.2.1 Wave Breaking Impact

As mentioned in section 1.2.2, both laboratory measurements and model simulations suggest that surface wave breaking (hereafter WB) could cause the losses of both energy and momentum from wave fields [Rapp and Melville, 1990; Melville et al., 2002; Sullivan et al., 2007]. Thus, wave breaking effects are parameterized as both a source of TKE injection at the surface boundary for the TKE transport equation and a body stress which transfers momentum to underlying current fields in the momentum transport equations. The 4.1.0 version of GOTM allows for the inclusion of WB-induced TKE injection, following the approach suggested by Craig and Banner [1994]. The WB-induced TKE injection is added to modify the upper boundary conditions for the TKE transport equation and is parameterized as u_{w*}^3 (the cube of friction velocities)

$$q_{wb,0} = m_0 \rho_w u_{w*}^3 \qquad (2\text{-}7)$$

where ρ_w is the seawater density, u_{w*} is the surface friction velocity on the water side, and m_0 is the wave energy factor, usually set as a constant of 100 suggested by Craig and Banner [1994]. However, for young wave regions (β<30, [Terray et al., 1996]), it is inappropriate to set the wave energy factor to be constant but rather a function of wave ages ($\beta = c_p/u_{*a}$, where c_p is the wave phase speed and u_{*a} is the air-side friction velocity). Thus, in this study m_0 is treated as a wave-age-dependent function following the approach of Kantha and Clay [2004]

$$m_0 = 4.053 * (0.037\beta^2 - 3.615/\beta) \quad (2\text{-}8)$$

with an upper bound (β=30) which indicates fully-developed wave fields.

The WB-induced momentum flux is parameterized as an additional body stress by He and Chen [2011]. Compared to the WB-induced TKE flux at the surface, He and Chen [2011] found that the WB-induced momentum flux works more effectively in enhancing the turbulent level and deepening the mixed layer. As a result, an extra term of wave-breaking-induced stress τ_{wb} is added to the momentum equations in this study. Following Sullivan et al. [2004, 2007], the vertical distribution of the wave breaking stress is expressed as

$$\tau_{wb}(z) = \langle A(z) \rangle \Delta z \qquad (2\text{-}9)$$

where $\langle A(z) \rangle$ is the momentum density (averaged over Δz at the depth of z). Based on this approach, He and Chen [2011] employed a curve fitting method and gave the vertical decay function as

$$\int_{-H}^{z} \langle A(z) \rangle dz / (\gamma \rho_a u_*^2) \approx e^{bz} \qquad (2\text{-}10)$$

where z is the upward vertical coordinate with $z=0$ representing the mean sea surface, b is a vertical decay coefficient, u_* is the atmospheric friction velocity, ρ_a is the air density, H is the water depth, and γ is the ratio of the wave-breaking stress to the total wind stress. This ratio is still an unknown function to be determined by the wind speeds and wave conditions. In the present study, we set γ to a constant value of 0.2, which is the same value used by He and Chen [2011] for Station Papa. In He and Chen [2011], the decay coefficient b only depends on the wind speeds. Cai et al. [2017] suggested that b should be a function of both wind speed and wave age for young wave regions. With introducing the wave-age-dependent momentum flux parameterization to the model simulations, the

model performance in simulating the SST is improved [Cai et al., 2017]. In this study, we apply a parameterization of the decay coefficient *b* suggested by Cai et al. [2017],

$$b = \begin{cases} b_1, & \beta \geq 30 \\ f(\beta) * b_1, & \beta < 30 \end{cases} \quad (2\text{-}11)$$

$$b_1 = 284.1 * e^{-0.2643 * U_{10}} \quad (2\text{-}12)$$

$$f(\beta) = 1.719 * e^{-0.0483 * \beta} + 2.113 * 10^{-11} * e^{0.7816 * \beta} \quad (2\text{-}13)$$

where U_{10} is the wind speed at 10 m above the mean sea surface, and β is the wave age. It should be noted that, since the impact of wave breaking is mainly confined to the uppermost water layer for fully-developed waves (β>30) [Sullivan et al., 2007], *b* is set to be the same as that for β=30 [Cai et al., 2017].

The inclusion of WB effects means that both the WB-induced TKE injection at the surface boundary and momentum fluxes to ocean current fields are considered. In this study, the WB-induced TKE is parameterized as an additional TKE injection to the TKE transport equation suggested by Craig and Banner [1994], with the wave energy factor optimized by wave age [Kantha and Clay, 2004]. The vertical distribution of the WB-induced momentum flux is parameterized using the scheme suggested by Sullivan et al. [2007] and He and Chen [2011], with the inclusion of wave age impact on the vertical decay coefficient [Cai et al., 2017]. The newly-modified GOTM also allows the input of the WB-induced TKE fluxes obtained from wave models to improve the model performance.

2.2.2 Stokes Drift Impact

The impact of Stokes drift on ocean currents is applied through two processes. *One* is the Coriolis Stokes force (CSF) caused by the interaction with the Coriolis effect. The other is the Langmuir circulation (LC) driven by the Stokes-vortex force. Here, we incorporate the CSF effect by adding an additional term, $f_c \times \vec{u}_s$, to momentum equations. Previous studies [e.g., Axell, 2002; Ardhuin and Jenkins, 2006; Li et al., 2013] demonstrated that the incorporation of Langmuir circulation in OGCMs generates deeper mixing. Following the approach suggested by Ardhuin and Jenkins [2006], we include the LC effect by adding an additional LC-induced shear production term (P_{lc}) to the TKE equations

$$P_{lc} = \mu_t\left(\frac{\partial u}{\partial z}\cdot\frac{\partial u_s}{\partial z} + \frac{\partial v}{\partial z}\cdot\frac{\partial v_s}{\partial z}\right) \qquad (2\text{-}14)$$

where μ_t is the vertical eddy viscosity, (u, v) are the current velocities in the eastward and northward directions respectively, and (u_s, v_s) are the Stokes drift velocities in the eastward and northward directions respectively.

Since the parameterization of Langmuir circulation depends sensitively on the shear of Stokes profile and the calculation of Coriolis-Stokes force depends on the magnitude and direction of vertical Stokes drift profile, the parameterization of the Stokes drift profile is important to model simulations. Previous studies usually assumed the vertical distribution of Stokes drift as an exponentially depth-decayed profile from the water surface [Polton et al., 2005; Li et al., 2013]. Breivik et al. [2014] proposed a new Stokes profile with a

deep-water approximation and suggested that the newly-proposed profile (Equation 2-15) has a better performance than the monochromatic profile, which is as expressed

$$u_s(z) = u_{s0}\frac{e^{2k_e z}}{1-8k_e z} \qquad (2\text{-}15)$$

where k_e represents the inverse depth scale and is estimated as $k_e \approx \frac{u_{s0}}{5.97V_s}$ where u_{s0} is the surface Stokes drift, and V_s is the Stokes transport. In addition to this parameterization of Stokes drift profile, the newly-modified GOTM also allows the directly input of Stokes profiles obtained from wave models or calculated by wave spectra.

Over all, the time-varying, depth-dependent (1D) momentum equations and k-ϵ equations incorporating the wave effects of wave breaking, Coriolis-Stokes force, and the Langmuir turbulence in GOTM are expressed as follows

$$\frac{\partial u}{\partial t} = \frac{\partial}{\partial z}\left(\mu_t \frac{\partial u}{\partial z}\right) + fv + fv_s + \tau_{wb,x} \qquad (2\text{-}16)$$

$$\frac{\partial v}{\partial t} = \frac{\partial}{\partial z}\left(\mu_t \frac{\partial v}{\partial z}\right) - fu - fu_s + \tau_{wb,y} \qquad (2\text{-}17)$$

$$\frac{\partial k}{\partial t} = \frac{\partial}{\partial z}\left(\frac{\mu_t}{\sigma_k}\frac{\partial k}{\partial z}\right) + (P + P_{lc}) + B - \epsilon \qquad (2\text{-}18)$$

$$\frac{\partial \epsilon}{\partial t} = \frac{\partial}{\partial z}\left(\frac{\mu_t}{\sigma_\epsilon}\frac{\partial \epsilon}{\partial z}\right) + \frac{\epsilon}{k}[c_{\epsilon 1}(P + P_{lc}) + c_{\epsilon 3}B - c_{\epsilon 2}\epsilon] \qquad (2\text{-}19)$$

2.3 Experimental Design for Process Studies

As discussed above, surface gravity waves impact the upper ocean mixing under fast-moving storms mainly by wave breaking, Langmuir circulation and Coriolis-Stokes force. A set of process studies are conducted in this study to examine the contributions of these wave-related processes on the upper ocean response to storms. Model results in the following eight different numerical experiments (Table 2.1) under two storm cases are presented in the next two chapters.

Exp-Alloff is set to be the reference baseline experiment which applies all the default settings of GOTM with the k-ϵ turbulence scheme. All the wave-related processes in this case are turned off, including the WB-induced TKE injection term which has been incorporated in GOTM. In experiments 2-4, the WB effect, the CSF effect, and the LC effect are turned on, respectively. Experiments 5-7 are designed to investigate the various combinations of two wave-related processes. All three wave-related processes are added to the model simulation in Exp-Allon to examine their cumulative modification of the upper ocean mixing. It should be noted that in any of numerical experiments that include the wave-breaking effect, both the WB-induced TKE injection and momentum flux are included. The Stokes drift profiles are given by Equation 2-15.

Table 2.1: List of numerical experiments for process studies.

Index	Experiments	Coriolis Stokes Force (CSF)	Langmuir Circulation (LC)	Wave Breaking (WB)
1	Exp-Alloff	No	No	No
2	Exp-CSF	Yes	No	No
3	Exp-LC	No	Yes	No
4	Exp-WB	No	No	Yes
5	Exp-CSF+LC	Yes	Yes	No
6	Exp-WB+CSF	Yes	No	Yes
7	Exp-WB+LC	No	Yes	Yes
8	Exp-Allon	Yes	Yes	Yes

Chapter 3

Wave Effects on Ocean Responses to Hurricane Arthur

In order to improve the model simulation of storm intensity, the comprehensive understanding of the upper ocean responses to storms is required. However, this kind of study is always limited by the deficiency of observations. As part of the Ocean Tracking Network (OTN), a glider was launched during the passage of Hurricane Arthur (2014). The storm moved across the Northwest Atlantic and made landfall in New Brunswick. These high-resolution underwater glider observations provide a unique opportunity to investigate ocean processes such as the current shear and wave-induced turbulence during the hurricane. In this chapter, we employ the newly-modified GOTM model to conduct 1D (i.e., depth-dependent) analyses of these physical processes, especially with surface gravity wave effects, under Hurricane Arthur conditions. The surface wave effects of wave breaking, the Coriolis-Stokes force and Langmuir circulation are included in GOTM based on the k-ϵ turbulent scheme. The process studies are conducted to identify the contribution of different wave-related processes in the case of Hurricane Arthur. Then *in situ* glider observations are used to assess the model performance in simulating the

upper ocean thermal responses with surface wave effects. The wave effects on ocean currents and the turbulence level of the upper ocean are also discussed in this chapter.

3.1 Overview of Observations

3.1.1 Synoptic Conditions for Hurricane Arthur

Hurricane Arthur formed east of Florida on July 3 2014 and made an initial landfall along the North Carolina coast as category 2 on the Saffir-Simpson hurricane wind scale. Hurricane Arthur accelerated northeastward with a translation speed of >10 m/s on July 4. This storm lost intensity due to much colder SST, leading to degradation to a tropical storm at 06:00 on July 5. Six hours later, Arthur weakened to an extratropical cyclone over the Bay of Fundy, with a larger radius of maximum winds and weaker maximum sustained winds. At the same time, the wind speeds over the glider region dramatically increased and reached a maximum of 22 m/s at 14:00 UTC with the center of Arthur about 300 km away from the glider track. The extratropical low continued northeastward toward the Gulf of St. Lawrence through July 6, producing gale-force winds and heavy rain over portions of Atlantic Canada.

The remote sensing data of SST were generated at approximately 4 km resolution using Advanced Very High Resolution Radiometer (AVHRR) instruments aboard NOAA polar-orbiting satellites. These remote sensing data were obtained from the National Oceanographic Data Center (NODC) AVHRR Pathfinder Project (https://www.nodc.noaa.gov/satellitedata/pathfinder4km53/). Since these satellite remote sensing data

of SST were sometimes not available due to high cloud coverage, we select the cloud-free observations on July 2 and July 6 2014 (Figure 3.1) to describe SST conditions of before and after Hurricane Arthur respectively. Before the passage of Hurricane Arthur, the spatial distribution of SST was nearly uniform (15.7±0.3℃) in the vicinity of the glider (Figure 3.1a, Table 3.1), which limits the impact of advection. Due to the passage of Hurricane Arthur, a significant SST cooling occurred with the SST of the glider region remarkably diminishing to ~12.1℃ (Figure 3.1b, Table 3.1).

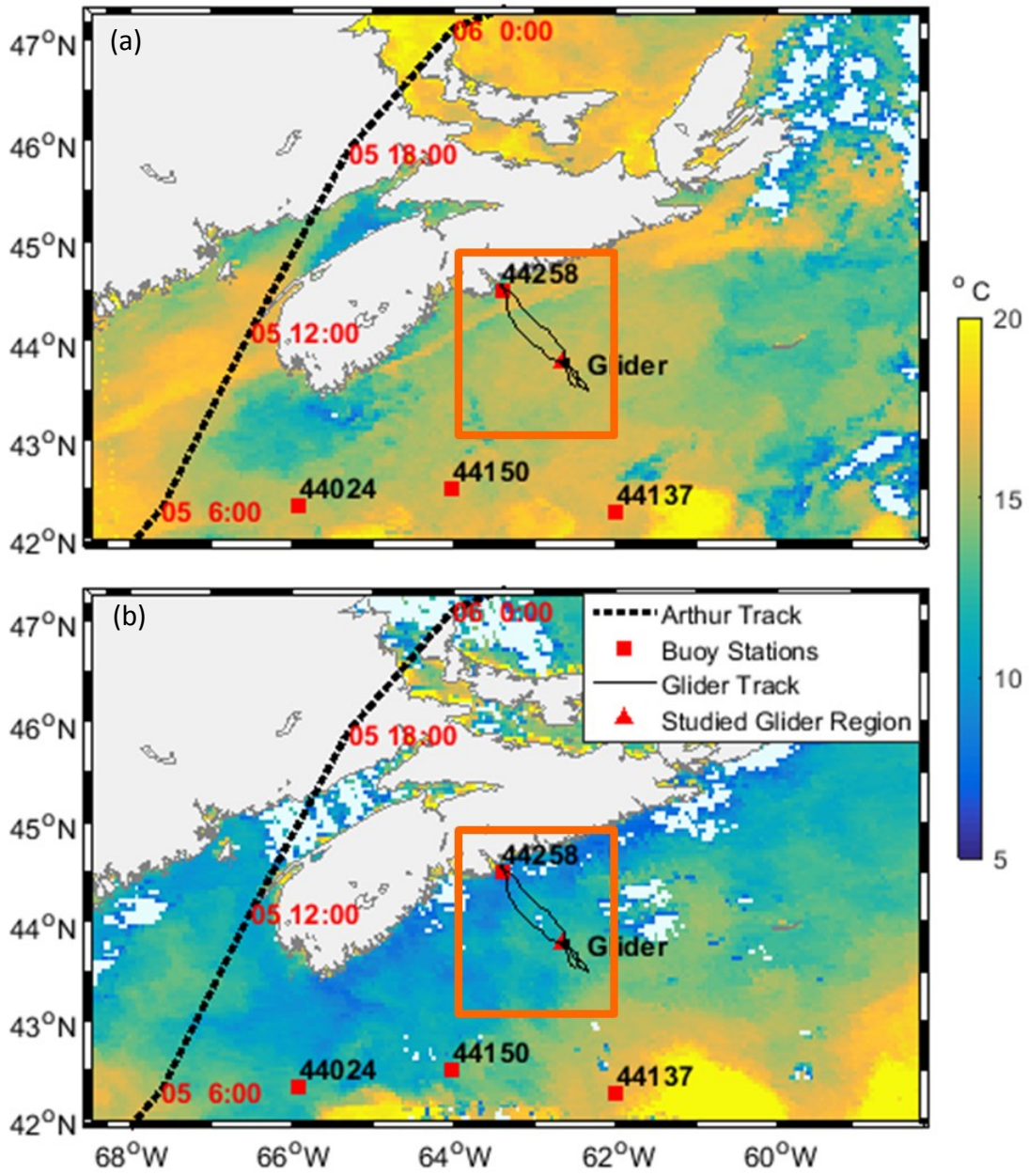

Figure 3.1: AVHRR SST distribution (a) before (July 2) and (b) after (July 6) Hurricane Arthur with the NHC best track (black dashed line labelled with July date and UTC time), positions of the NDBC buoys (red squares), the OTN200 underwater glider track (thine black line), and the glider location during Hurricane Arthur (red triangle).

Table 3.1: The mean values, standard deviations and mean absolute differences of the satellite remote sensing data of SST in the vicinity of the glider with the radius of 80 km.

SST (℃)	Average	Standard Deviation	Mean Absolute Difference
Pre-Arthur	15.72	0.32	0.24
Post-Arthur	12.13	1.26	0.76

Differences in satellite remote sensing data of SST between July 4 (pre-storm) and July 6 (post-storm) reveal the regional pattern of SST cooling over the Scotian Shelf (Figure 3.2a). The largest cooling (>5 ℃) occurred parallel to the 100 m isobaths over the inner shelf of Scotian Shelf. The SST cooling over the middle to outer shelf within the 200 m isobaths was relatively weak with the area-mean cooling of 2.5-4 ℃ cooling.

3.1.2 Oceanic Observations

The meteorological and oceanic conditions at four buoys (44024, 44150, 44137, and 44258) deployed by the National Data Buoy Center (NDBC) were measured near the glider track (Figure 3.2 b-d). Buoy 44258 is not shown here due to the missing SST data during Hurricane Arthur. The peak wind speed was recorded to be ~21.5 m/s at 44024, with the minimum air pressure of 992 mb at 08:00 UTC on July 5. At buoys 44024 and 44150, the SST dropped rapidly by 3-4 ℃ during Hurricane Arthur. The significant SST cooling did not occur at 44137, since 44137 was out of the region where Hurricane Arthur influenced directly. As air temperature cooled more quickly than SST, observed air temperatures were less than SSTs shortly after the passage of Hurricane Arthur, indicating the air-sea sensible heat fluxes from the ocean to the atmosphere. Wave

conditions were significantly modified as Hurricane Arthur approached, with significant wave heights increasing from <2 m to 5-7.5 m.

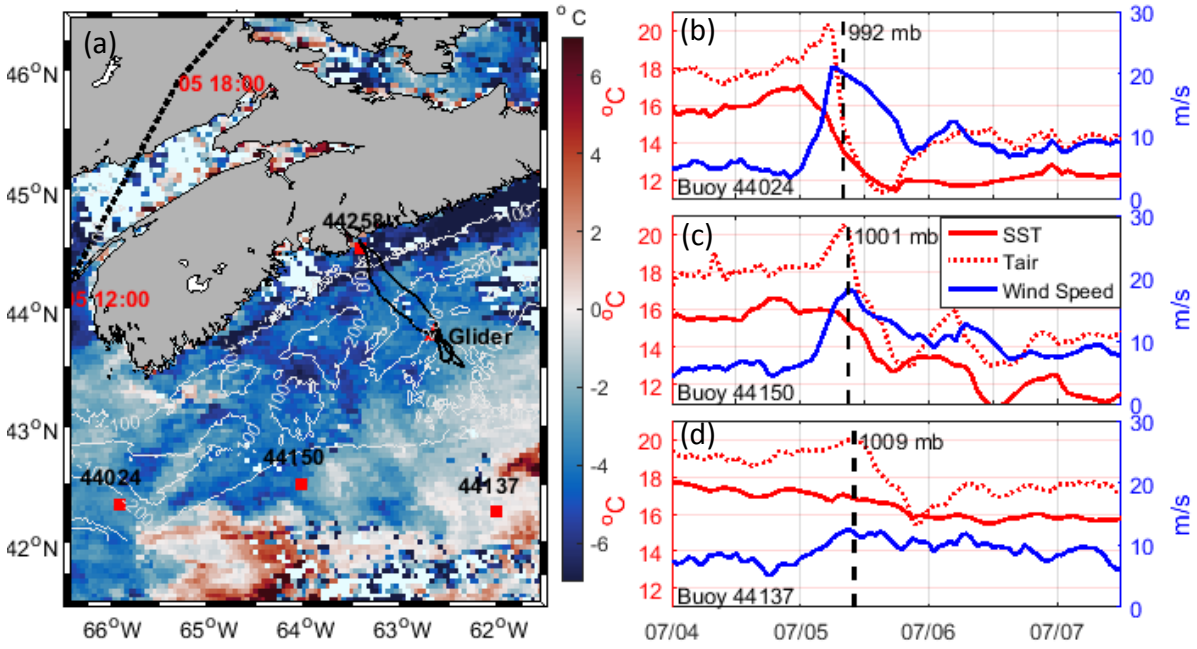

Figure 3.2: (a) Spatial distribution of SST difference between July 6 (post-storm) and July 2 (pre-storm) with the same legend as Figure 3.1. (b-d) Buoy observations of SST (solid red), air temperature (dashed red), and wind speed (solid blue) with vertical black dashed line indicating the time of minimum air pressure.

The vertical profiles of observed temperature and salinity made by the Teledyne Webb Research Slocum electric underwater glider (hereafter glider) were obtained from the website of http://gliders.oceantrack.org/. In late June 2014, the glider was deployed off Halifax Harbor and dived to depths varying between 5 m and 200 m over the Scotian Shelf (Figure 3.3a) with the mean horizontal speed of ~1 km/hour. The glider made measurements of ocean physical, chemical and biological conditions of the shelf water on a time-scale of seconds and a vertical-scale of ~0.25 m. On July 5, the glider entered the

area directly influenced by Hurricane Arthur and began to track a small triangle pattern between Emerald Bank and Emerald Basin, in order to capture upper ocean modifications by Hurricane Arthur. These high-resolution glider data provide a valuable opportunity to assess the role of surface gravity waves on the 1D-related upper ocean responses, including the mean current shear and the wave-induced turbulence to storm winds with the newly-modified GOTM.

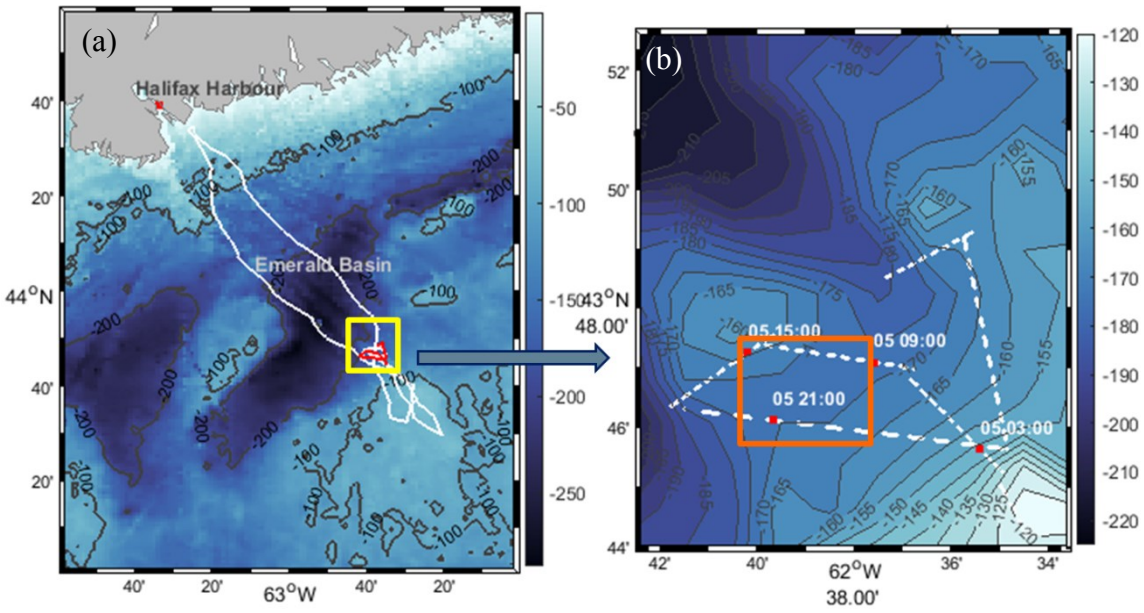

Figure 3.3: (a) The glider track (the white solid line) from June 26 to July 15, 2014. (b) Enlarged track (the white dashed line) during the passage of Hurricane Arthur over the central Scotian Shelf with the red box denoting the available glider observation used to assess the model simulations. The bathymetry data were extracted from Smith and Sandwell [1997].

Previous studies demonstrated that the vertical hydrographic profiles have a three-layer vertical distribution on the Scotian Shelf in summer illustrated by underwater glider observations [e.g., Shan, 2016]. The three-layer structure features a relatively warm

surface layer (usually >15°C) due to the seasonal positive atmospheric heat flux to the ocean, a cold intermediate water layer at the seasonal thermocline, and warmer but saltier bottom waters that invade from beyond the shelf break. Before the arrival of Hurricane Arthur, the glider measured the temperature within the upper warm layer of ~16 ℃ at the start of July 5, with a shallow summer mixed layer of about 13±2 m (Figure 3.4a). Noh et al. [2011, 2016] suggested that the additional mixed layer deepening by the LC effect is more significant in the ocean with a shallow OML than the ocean with a deep OML. The temperature gradient was relatively sharp (e.g. the temperature changed ~7 ℃ in depth of 5 m) between the surface warm layer and the intermediate cold layer in summer. By the end of July 5, Hurricane Arthur significantly modified the temperature structure of the upper ocean (Figure 3.1b and 3.4a), with the upper ocean temperature cooling by more than 2 ℃. The mixed layer depth deepened to ~25 m. The stratification of the upper ocean diminished (Figure 3.4c). The heat loss from the upper ocean was transported to warm the water beneath the mixed layer, i.e., depths of 17-30 m (Figure 3.4a). After the passage of Hurricane Arthur, the wind forcing conditions gradually returned to the previous state. By comparison, oceanic thermal responses were somewhat sustained for about three days before starting to recover, with minimum SST decreasing to ~11 ℃ and the maximum OML up to ~30 m (illustrated by glider observations, but not shown here). These oceanic responses could be attributed to processes such as intensified oceanic vertical mixing within the thermocline, cooler water entrainment through the base of mixed layer, air-sea heat exchanges, and horizontal current advection [e.g., Price 1981; Ginis 1995]. It should be noted that contributions of these processes may change under

different storms with different characteristics (e.g. translation speed, intensity), for different oceanic conditions (e.g. the stratification, mesoscale currents), and for different stages (e.g., during the relaxation stage, more 3D dynamics, such as the horizontal current advection or the upwelling).

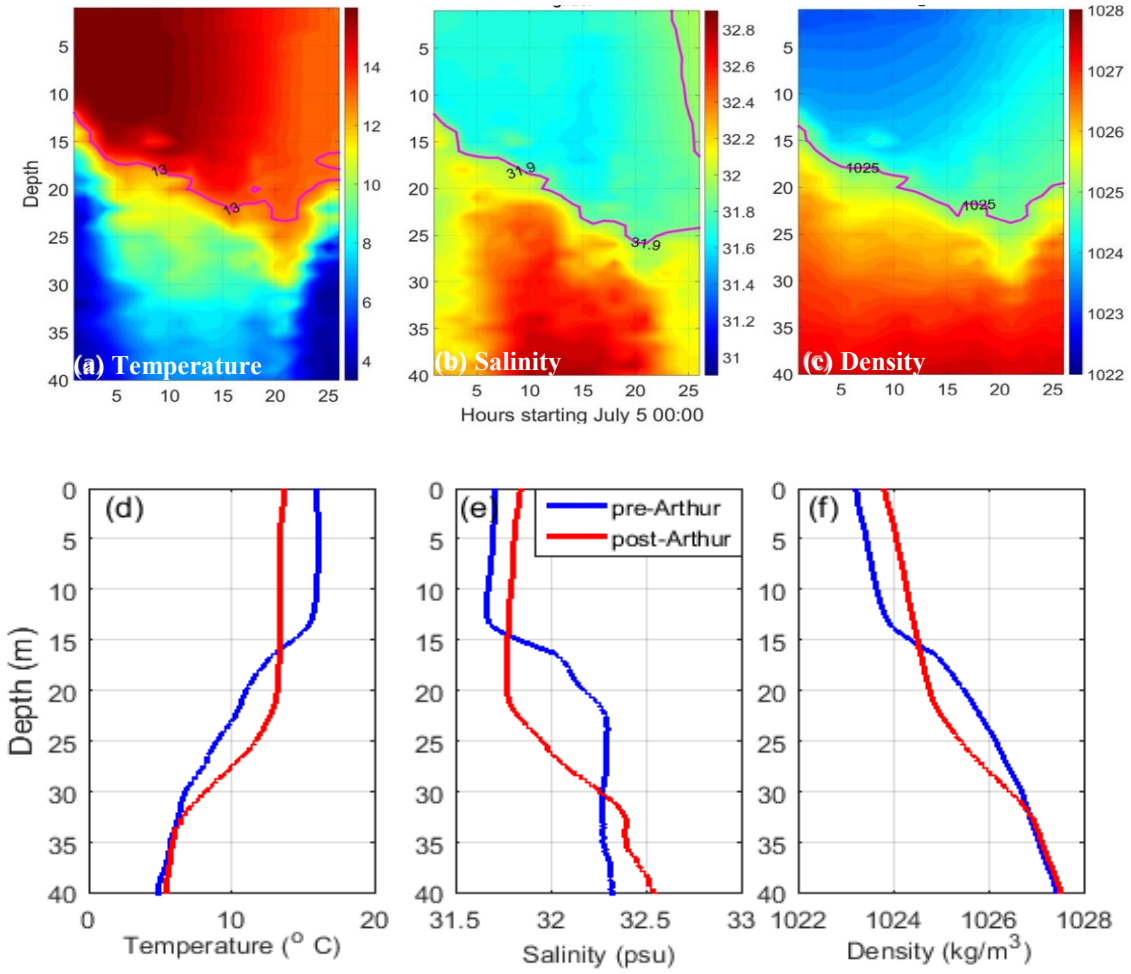

Figure 3.4: Time-depth distributions of (a) temperature, (b) salinity, and (c) density evolution of underwater glider observations during Hurricane Arthur (00:00 on July 5 to 00:00 on July 6, 2014). Vertical profiles of (d) temperature, (e) salinity, and (f) density by glider measurements before Hurricane Arthur at 05:00 on 5 July 2014 (blue) and after Hurricane Arthur at 21:00 on 5 July 2014 (red).

3.2 Model

3.2.1 Justification for 1D Model Simulation

In this study, the 1D GOTM was applied to the case of Hurricane Arthur. It should be noted that the 1D (i.e., depth-dependent) model does not reproduce the entire features of observed ocean responses, since the 1D model does not include 3D dynamics especially during the relaxation stage. Nonetheless, the 1D GOTM should be able to simulate the locally generated near-inertial mixed layer currents, associated shear instabilities which induce significant vertical mixing especially near the base of the mixed layer, and subsequently thermocline with colder water entrainment leading to the upper ocean cooling and OML deepening. Furthermore, the surface gravity waves affect the upper ocean response to storms by modifying vertical mixing, which can also be reproduced by the newly-modified 1D GOTM. Thus, this 1D model can be used to examine the surface wave effects on the upper ocean responses to Hurricane Arthur, especially the current shear in the vertical direction, wave-induced turbulence and associated oceanic thermal responses, and identify the contribution of each wave-related process through process studies.

A scale analysis (Table 3.2) was also conducted for Hurricane Arthur. It was found that the upper ocean responses are basically one dimensional dynamics dominated at the forced stage with following reasons. Firstly, Hurricane Arthur was a fast-moving storm as it passed by Atlantic Canada. Previous numerical studies suggested the dominant role of 1D (i.e., depth-dependent) dynamics in the upper ocean responses to rapidly-moving storms at the early forced stage. Secondly, Sheng et al. [2006] obtained the similar spatial

distribution of SST cooling under an idealized comparatively fast-moving storm by two experiments with and without vertical advection effects. They suggested that the vertical mixing plays a dominate role in SST changes including the rightward bias for Hurricane Juan which was a fast-moving storm. Yablonsky and Ginis [2009] conducted simulations of oceanic responses to storms with variant translation speeds by both 1D and 3D versions of the Princeton Ocean Model (POM). Their results showed that when the storm translation speed is >5 m/s, 1D simulations are similar to those of 3D, especially for the first 12 hours during the forced stages. Thirdly, the translation speed of Hurricane Arthur during July 4-7 was 10.5 m/s on average (much higher than 5 m/s), which allows us to expect the dominant role of 1D dynamics in the upper ocean responses at the early forced stage.

The scale analysis also suggests the ocean responses to Hurricane Arthur as the first order of one-dimensional processes. The scale analysis, following the approach suggested by Price et al. [1994], is conducted to several storm cases [e.g., Dickey et al., 1998; Shay et al., 2000] to isolate the factors which make the most contribution to determine the upper ocean responses. The Best Track Data Sets from National Hurricane Center (NHC, http://www.nhc.noaa.gov/data/) are used for the scale analysis. The scale parameters are shown in Table 3.2. In this case, the non-dimensional storm speed S is O(1), which indicates the roughly aligned rotation rate of wind stresses and inertial transports [Price 1981] and the strong near-inertial motion included in the response of upper-ocean currents. The Burger number (0.006) is smaller than previous studies (e.g., 0.02 for Gloria [Price et al., 1994], 0.01 for Hurricane Felix [Dickey et al., 1998]), which

indicates weak pressure coupling between mixed layer currents and thermocline currents. Thus, we expect that the non-local dynamics during the relaxation stage, such as divergence-induced upwelling, are not important at the forced stage, and the decay rate of energy within the mixed layer is small. The small estimated isopycnal displacement ($\tilde{\eta} = 2.05\ m$) also support this expectation. In addition, the Rossby number for mixed layer currents (Q=0.08) is also smaller than Hurricane Felix and Gloria (Q=0.2), which suggests the minor effects of nonlocal or advective processes during the forcing and early decay stages.

Table 3.2: List of scale parameters. These variables are calculated based on the NHC data at the moment closest to 14:00 UTC on July 5 when the eye center of Hurricane Arthur was closest to the glider region.

External parameters			
Translation speed, $U_H, m/s$	10	Radius of max wind, R_{max}, km	61.5
Wind Stress, $\tau, N/m^2$	2.14	Coriolis frequency, f, s^{-1}	1.01×10^{-4}
Reduced gravity $g' = \frac{g\Delta\rho}{\rho_0}, m/s^2$	3.81×10^{-2}	OML depth, h_{ml}, m	25
Scales for the independent variables			
Across-track scale R_{max}, km	61.5	Along-track scale $L_i = \frac{U_H}{f}, km$	98.5
Scales for the dependent variables			
OML current, $U_{ml} = \frac{2\pi R_{max}}{\rho_0 h_{ml} U_H}, m/s$	1.5	Isobar displacement, $\tilde{\eta} = \frac{\tau}{\rho_0 f U_H}$, m	2.05
Nondimensional variables			
Storm speed $S = \frac{\pi U_H}{4 f R_{max}}$,	1.25	Burger number $B = \frac{g' h_{ML}}{4 f^2 R_{\max}^2}$,	0.006
Rossby number $Q = \frac{\pi}{\rho_0 h_{ML} U_H f}$,	0.08		

3.2.2 Model Domain and Initialization

As discussed above, the large translation speeds of Hurricane Arthur and the scale analysis suggest that the observed oceanic responses are dominated by 1D processes at the early forced stage and thus can be primarily reproduced by 1D (depth-dependent) GOTM simulation. However, though the OTN glider was reset to track a small triangle pattern during the passage of Hurricane Arthur, the measurement was not strictly one dimensional due to the horizontal movement of the glider. To minimize the effect of the horizontal movement of the glider, we select the glider measurements in a box region (Figure 3.3b) to assess the GOTM simulation. The box region was chosen based on the following conditions: (a) generally uniform bathymetry (170 $\pm$5 m), (b) the sufficiently small scale (3.2×3.2 km) compared to Hurricane Arthur's scale, and (c) in the period of the storm forced stage. The red rectangle box region shown in Figure 3.3b is treated as the location at which the 1D GOTM is applied. The glider observations within the box region are used to assess the GOTM simulations.

The hydrographic field of our simulation is initialized using the vertical profiles of observed temperature and salinity at 09:00 on July 5 2014. Due to the horizontal speeds of the glider during sampling, the glider data were interpolated in 0.1 m in the vertical direction every 10 mins. The GOTM model is integrated from 09:00 UTC on July 5 2014 with the vertical resolution of 0.1 m. The forcing and wave conditions for the GOTM simulation will be validated in the next section.

3.2.3 Validation of the Wind, Heat and Wave Conditions

Due to the lack of meteorological measurements, the hourly model outputs from Rutgers University Weather Research and Forecast model (hereafter RUWRF, http://tds.maracoos.org/thredds/catalog.html) are used to describe the forcing conditions for the GOTM model in this study. The RUWRF model outputs include the hourly wind speeds for momentum forcing, and short-wave radiations, relative humidities, cloud covers, air pressures, air temperatures for heat forcing. The spatial resolution for RUWRF is 9 km which is acceptable to describe the storm forcing structure. We use the RUWRF outputs closest to the location where the GOTM is applied as model forcing conditions. To validate RUWRF model outputs, we compared them with buoy observations near the glider track. The wind speeds, air pressures and sea surface net heat fluxes are validated with observations. The root mean square errors (RMSE) are relatively small and the correlation coefficients (CC) are larger than 0.8 (Figure 3.5 and 3.6, Table 3.3 and 3.4). It should be noted that the observed wind speeds at buoys are the hourly averaged results, while the RUWRF wind speeds are the instantaneous model outputs. This may explain the differences of wind speed peaks between RUWRF model outputs and buoy observations. The following results for validation are all statistically significant.

Table 3.3: Root mean square errors (RMSE) and correlation coefficients (CC) for wind speeds (WSPD) and air pressures at the sea level (SLP)

Buoys	RMSE_WSPD (m/s)	CC_WSPD	RMSE_SLP (mb)	CC_SLP
44137	2.01	0.68	4.89	0.93
44150	2.28	0.87	5.44	0.93
44258	2.18	0.90	6.36	0.95
Average	2.16	0.82	5.56	0.94

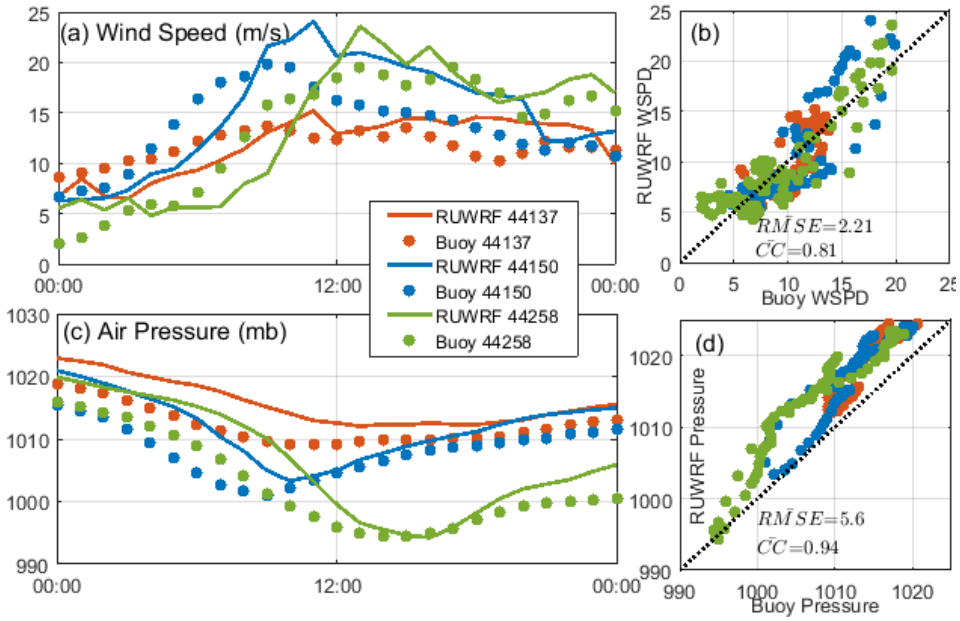

Figure 3.5: Time series of observed (dots) wind speeds (upper panel) and air pressures at the sea level (lower panel) in comparison with RUWRF model outputs (solid curves) at buoys 44137 (red), 44150 (blue) and 44258 (green) near the glider track during the passage of Hurricane Arthur on July 5, 2014.

Table 3.4: Root mean square errors (RMSE) and correlation coefficients (CC) for net heat fluxes

Buoys	RMSE_HeatFlux (W/m^2)	CC_HeatFlux
44024	116.49	0.94
44137	130.88	0.93
44150	128.01	0.93
Average	125.13	0.93

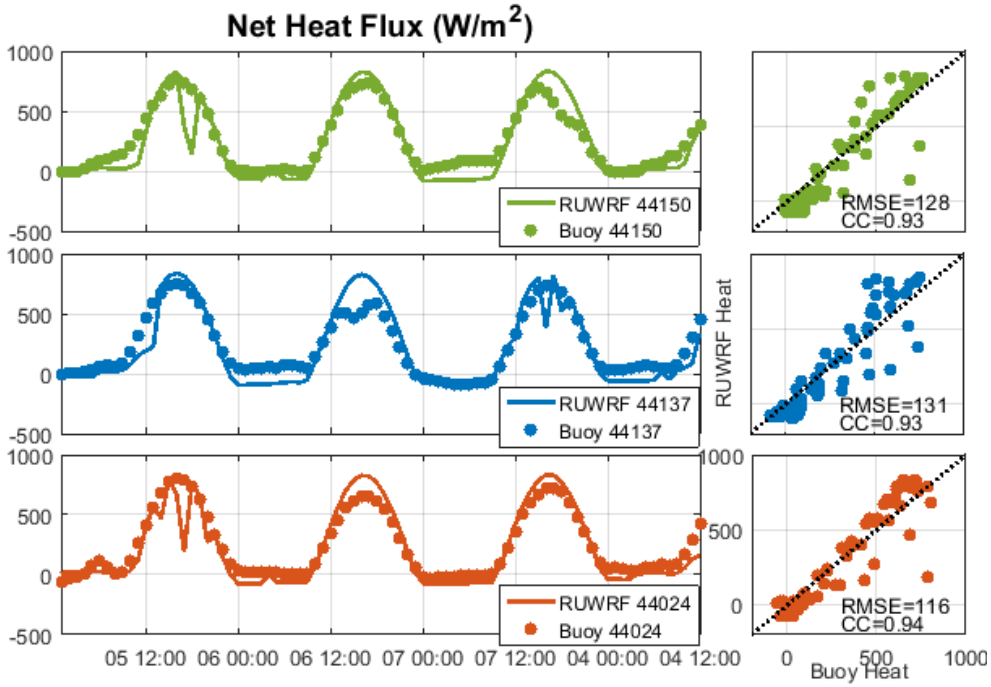

Figure 3.6: Time series of observed (dots) sea surface net heat fluxes in comparison with RUWRF (solid curves) at buoys 44150 (green), 44137 (blue) and 44024 (red) near the glider track during the passage of Hurricane Arthur on July 5, 2014.

The wave conditions over the location where the GOTM model is applied are specified based on the 3-hourly model outputs from WAVEWATCHIII (hereafter WW3,

ftp://ftp.ifremer.fr/ifremer/ww3/HINDCAST/) conducted by the French Research Institute for Exploitation of the Sea (hereafter IFREMER) with the spatial resolution of 9 km. These modelled wave conditions are also validated with observations at the three buoys near the glider track in terms of the significant wave height (H_s), the peak wave period (T_p), the surface Stokes drift (U_{s0}), and the Stokes drift transport (T_{U_s}, Figure 3.7 and Figure 3.8, Table 3.5 and 3.6). The WW3 outputs overall agree with the buoy observations with the mean CC of reaching more than 0.88. In the validations of significant wave heights and peak wave periods, the WW3 model outputs have better agreement with observations at buoy 44150 than at other two buoy locations. Noticeable differences between simulations and observations are detected at buoy 44258 which was located near Halifax Harbor with the water depth of ~60 m, which is much shallower than those at two other buoys.

Table 3.5: Root mean square errors (RMSE) and correlation coefficients (CC) for significant wave heights (H_s) and peak wave periods (T_p)

Buoys	RMSE_H_s (m)	CC_H_s	RMSE_T_p (s)	CC_T_p
44137	0.49	0.97	1.03	0.90
44150	0.47	0.97	0.72	0.93
44258	0.54	0.95	1.03	0.81
Average	0.50	0.96	0.93	0.88

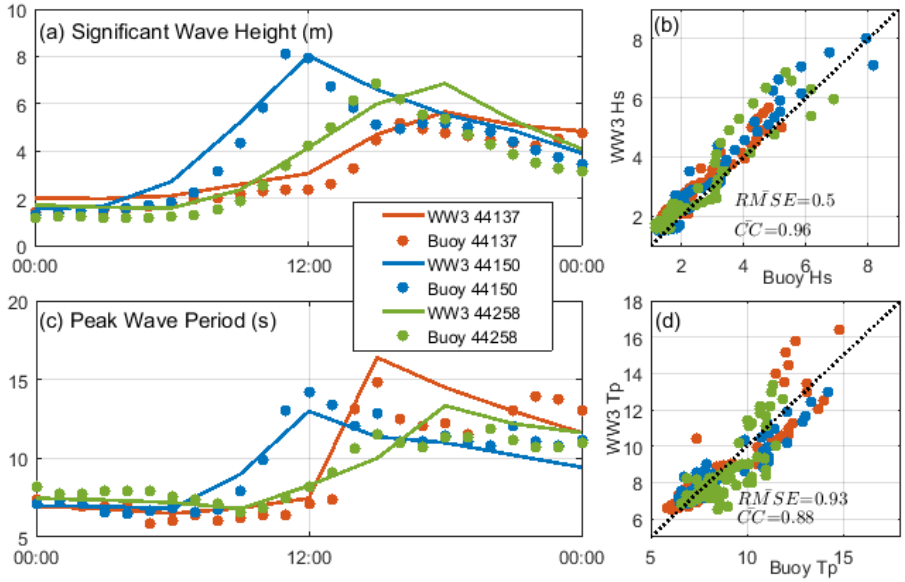

Figure 3.7: Time series of observed (dots) significant wave heights (upper panel) and peak wave periods (lower panel) in comparison with WAVEWATCH III (solid curves) at buoys 44137 (red), 44150 (blue) and 44258 (green) near the glider track during the passage of Hurricane Arthur on July 5, 2014.

Table 3.6: Root mean square errors (RMSE) and correlation coefficients (CC) for surface Stokes drifts (U_{s0}) and Stokes transports (T_{U_s})

Buoys	RMSE_U_{s0} (m/s)	CC_U_{s0}	RMSE_T_{U_s} (m^2/s)	CC_T_{U_s}
44137	0.03	0.90	0.18	0.68
44150	0.02	0.92	0.21	0.78
44258	0.03	0.93	0.22	0.77
Average	0.03	0.92	0.20	0.76

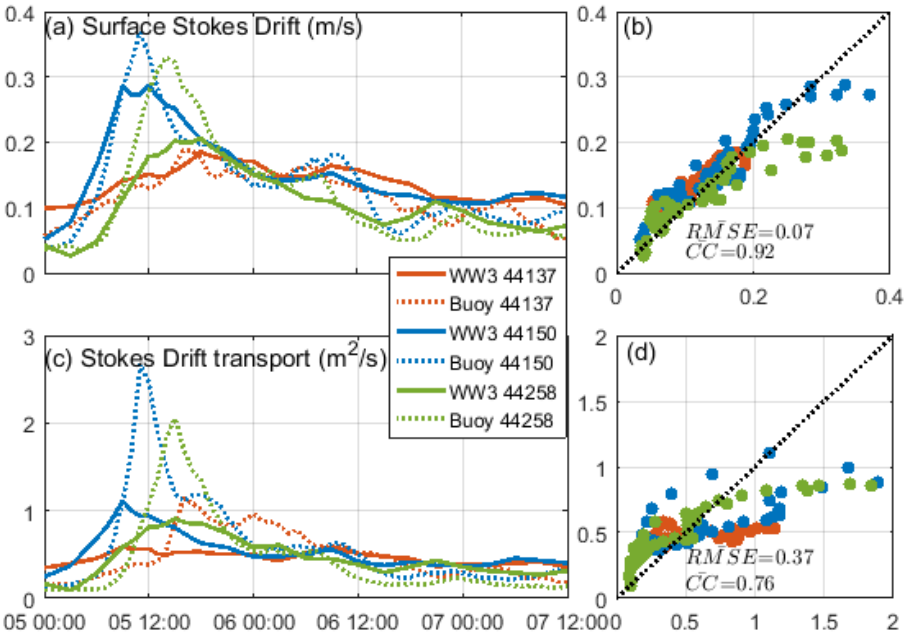

Figure 3.8: Time series of observed (dash) surface Stokes drifts (upper panel) and Stokes drift transports (lower panel) in comparison with WAVEWATCH III (solid) at buoys 44137 (red), 44150 (blue) and 44258 (green) near the glider track during the passage of Hurricane Arthur (July 5-7, 2014).

The model forcing and wave conditions taken before and after the passage of Hurricane Arthur in the study area are illustrated in Figure 3.9. Before Hurricane Arthur, the wind speeds at 10 m height above the sea surface were less than 8 m/s, with significant wave heights less than 2 m and surface Stokes drift less than 0.1 m/s. After 06:00 on July 5, the average wind speeds increased significantly from ~10 m/s (19 knot) to a maximum wind of ~22 m/s (43 knot) at 14:00 on July 5. The wind speeds persisted around 20 m/s (39 knot) till the end of the day (Figure 3.9). The maximum significant wave heights exceeded ~7.5 m, along with surface Stokes drift velocity that reached a maximum of ~0.25 m/s. After July 6, Hurricane Arthur continued moving further

northeastward, and winds and wave conditions over the study region weakened back to their previous before-storm levels.

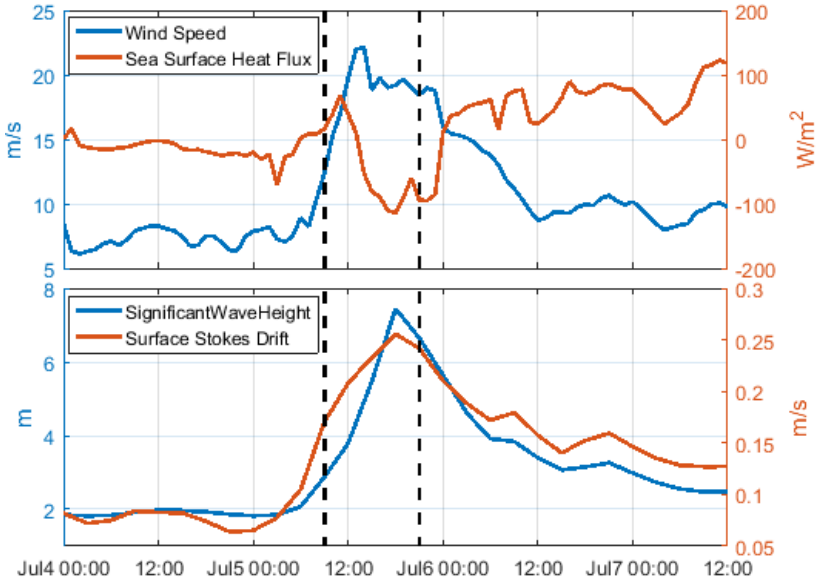

Figure 3.9: Time series of (a) wind speeds, (b) surface heat fluxes, (c) significant wave heights, (d) surface Stokes drifts in the glider region from 00:00 on July 4 to 12:00 on July 7, 2014. The thick black dashed line denotes the initial time of GOTM (09:00 on July 5) and the thin black dashed line denotes the time when the glider swam out of the studied box region

3.3 Model Results

3.3.1 Wave Effects on Thermal Responses to Hurricane Arthur

Figure 3.10 exhibits the time evolution of temperature differences between model simulations and glider observations. The temperature evolution produced by the simulation without wave effects (Exp-Alloff) indicates a significant underestimation of the upper ocean cooling in the OML. This underestimation of upper ocean cooling intensifies with the time evolution, ending up being 0.8 ℃ or 37% less than the

observations at 21:00 on July 5 (Figure 3.10a). The inadequate cooling is likely attributed to the inadequate mixing of the upper ocean due to the exclusion of surface gravity wave effects [e.g., Sullivan et al., 2007; Wu et al., 2015]. This inadequate mixing can also result in the underestimation of the OML deepening [e.g., Emanuel, 2001; Pasquero and Emanuel, 2008]. The simulated OML in Exp-Alloff ends up being 20.6 m, which is 2.3 m shallower than the observation. In this study, the OML is defined as the depth at which the temperature is 1 ℃ less than SST [Lamb et al., 1984; Wagner et al., 1996].

With the inclusion of wave effects, the underestimation of both the upper ocean cooling and the OML deepening is reduced (Figure 3.10b-h). The simulations made by Exp-Allon agree the best with glider observations. Ahead of the storm eye center, wave effects (Exp-Allon) diminish the underestimation by over 50% at 14:00 on July 5 (Figure 3.10h). Simultaneously, wave effects contribute to enhance the OML deepening. The simulated OML of Exp-Allon is 2.5 m deeper than that of Exp-Alloff at the arrival of storm eye center at 16:00 on July 5. After the passage of the eye center, the simulation with wave effects (Exp-Allon) confines the upper ocean temperature biases to ~0.25 ℃ and deepens the OML to 22.6 m which is a slight underestimate compared to observations.

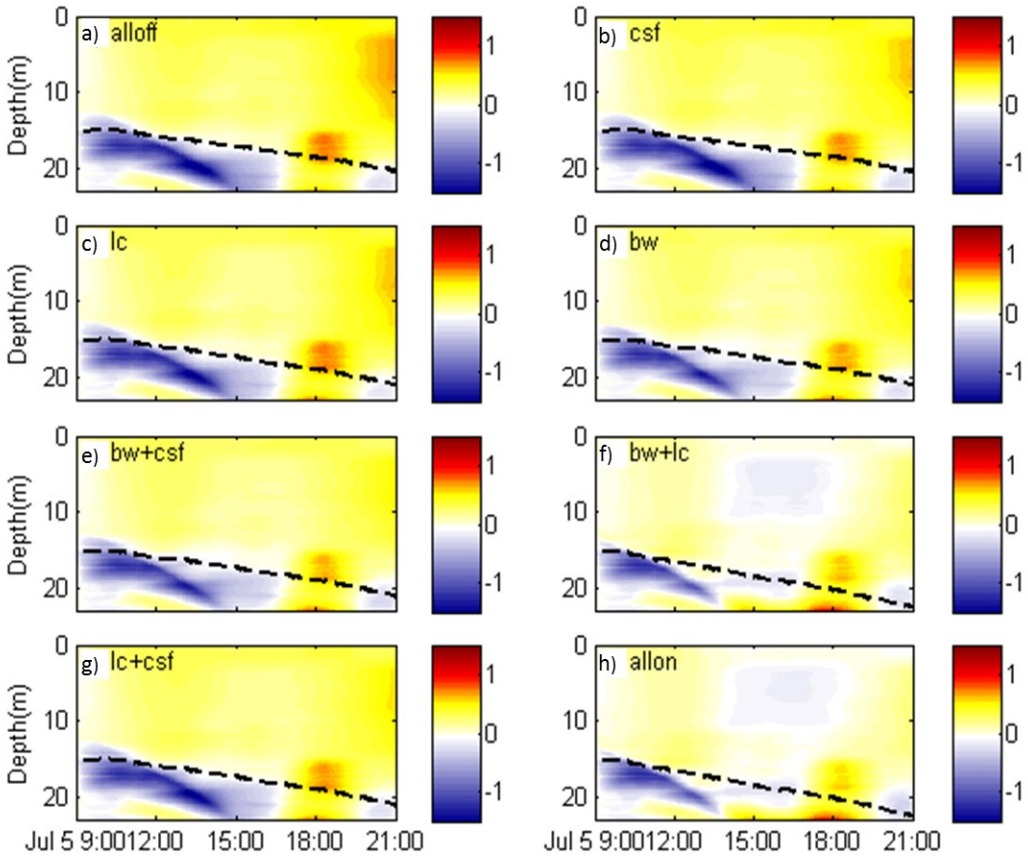

Figure 3.10: Time-depth distributions of temperature differences between simulated results and measurements in cases of: (a) Exp-Alloff (no wave effects), (b) Exp-CSF (only influence of CSF), (c) Exp-LC (only influence of LC), (d) Exp-WB (only influence of wave breaking), (e) Exp-WB+CSF (influences of CSF and wave breaking), (f) Exp-WB+LC (influences of LC and wave breaking), (g) Exp-LC+CSF (influences of CSF and LC), (h) Exp-Allon (all wave effects). The black dashed line denotes the OML.

The selected vertical profiles of ahead-of-eye-center temperature changes are compared to glider observations (Figure 3.11). The ahead-of-eye-center temperature cooling refers to the temperature changes occurring before the arrival of the storm eye center. Glenn et al. [2016] demonstrated the importance of ahead-of-eye-center vertical shear-induced mixing and the associated rapid temperature changes in improving the prediction of storm intensity. Significant ahead-of-eye-center SST cooling (3.5 ℃)

occurred at 44024, which was 64% of the total cooling (5.5 ℃). Based on the glider observation, the upper ocean temperature changes were minor before 12:00 UTC when wind speed was increasing but still <20 m/s. The air pressure for the glider region reached minimum (1002 mb) at 16:00 on July 5, and the glider swam out of the studied box after that. Thus, simulations of the ahead-of-eye-center temperature changes are compared to glider observations during this period which is still under the storm forced stage. Here, we only illustrate the temperature change at 14:00 UTC (Figure 3.11) for example when the wind speed reached maximum.

Figure 3.11 shows the vertical profiles of temperature changes which are the differences between temperature profiles at 14:00 and at 09:00 on July 5. The observations indicate that the storm-induced cooling in the initial OML was ~0.6 ℃ and maximum warming below the initial OML reached ~2.1 ℃. Wave effects increase the upper cooling from ~0.2 (Exp-Alloff) to ~0.6 ℃ (Exp-Allon) which is three times as much as that of Exp-Alloff. Simultaneously, compared to the Exp-Alloff, more heat is transported below the initial OML with the OML ~2 m deeper in Exp-Allon. It should be noted that wave age effects modify the vertical temperature changes (Figure 3.12), e.g., ~0.1 ℃ (or 17% of the observation) more temperature cooling occurring in the upper 13 m water. The wave age effects affect mainly through reducing the vertical decay rate of WB-induced momentum flux, which reaches a minimum with the wave age of 16 [Cai et al., 2017]. Though modifications of SST cooling and OML deepening by wave effects are comparatively small values, they are considered important since previous coupled air-ocean model studies demonstrated that even small shifts in SST and vertical stratification

can have significant impacts on the storm intensity [Emanuel, 2003; Schade and Emanuel, 1999].

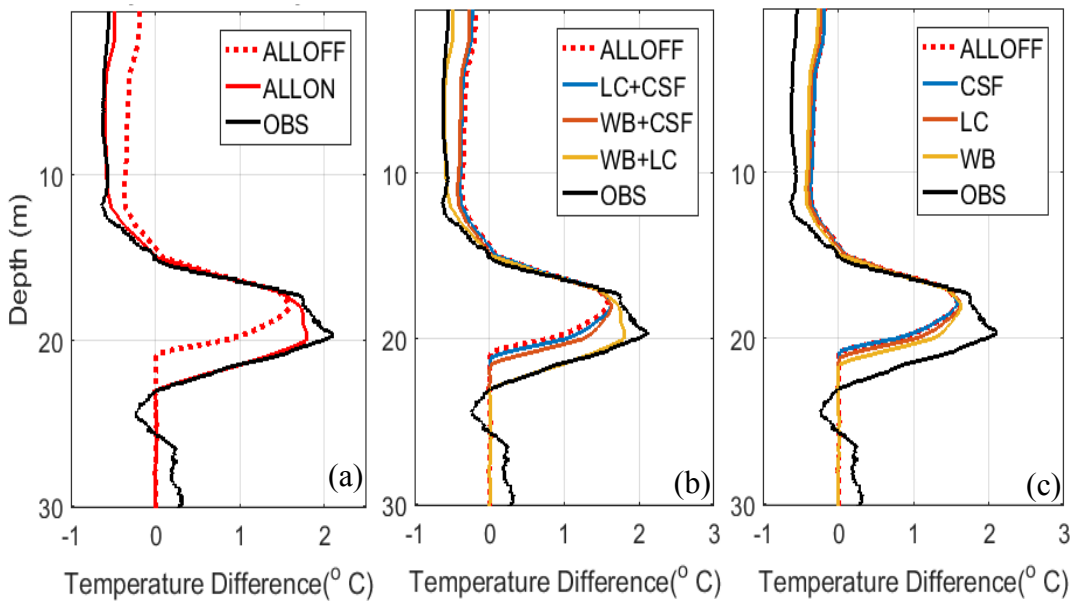

Figure 3.11: Vertical profiles of simulated (color curves) and measured (solid black curves) temperature changes between 14:00 and 09:00 on July 5. (a) The comparison between Exp-Allon and Exp-Alloff, (b) the comparison among the simulations with combinations of two wave-related processes, (c) the comparison among the simulations with single wave-related processes.

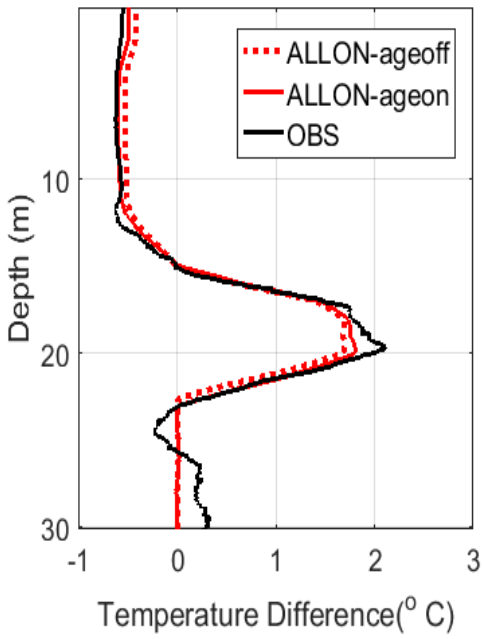

Figure 3.12 Wave age effects in the respect of vertical temperature change profile between 09:00 and 14:00 UTC on July 5. The simulated results are shown in red with the solid curve denoting simulation with wave age effects and dashed curve without wave age effects, and glider observations are shown in solid black.

The cumulative effects of these improvements modify the heat budget of the upper ocean. Following Large et al. [1986], we introduce the depth-integrated heat content anomaly (DIH) for vertical intervals of net cooling ([0, 15 m]) and net warming ([15, 23 m]) to quantify the cumulative effect of the simulated bias (Table 3.7). Without wave effects (Exp-Alloff), the heat loss of the upper ocean is ~16.6 MJ/m^2, which is only about a half of the observed heat loss. With all wave effects (Exp-Allon), the heat loss doubles and reaches 30.7 $\mathrm{MJ/m^2}$, which is much closer to the glider observation. In the interval of net warming ([15, 23 m]), the heat gain is extended over 50% with the inclusion of wave effects.

Table 3.7: Depth integrated heat anomaly of the observations and simulations for the depth intervals of 0-15 m ($DIH_{0\text{-}15}$), and 15-23 m ($DIH_{15\text{-}23}$). In this table, DIH is calculated following this equation: $DIH = \rho_{water} c_{pw} \int_{z_1}^{z_2} \left(T_{end}(z) - T_{initial}(z)\right) dz$ [Large et al., 1986].

	$DIH_{0\text{-}15}$ (MJ/m^2)	$DIH_{15\text{-}23}$ (MJ/m^2)
Exp-Alloff	-16.6	24.4
Exp-CSF	-16.5	24.3
Exp-LC	-18.8	26.5
Exp-WB	-20.6	28.4
Exp-CSF+LC	-18.6	26.3
Exp-WB+ CSF	-20.4	28.2
Exp-WB+ LC	-30.9	38.7
Exp-Allon	-30.7	38.5
OBS	-33.4	40.5

The vertical profiles of temperature changes shown in Figure 3.11 qualitatively exhibit the contribution of each combination of wave-related processes. With the inclusion of single wave-related processes, i.e. Exp-CSF, Exp-LC and Exp-WB, the simulations of the upper ocean temperature change are slightly improved (Figure 3.11c). With the inclusion of two combined wave-related processes, i.e., Exp-WB+CSF, Exp-WB+LC and Exp-CSF+LC, simulations of the upper ocean cooling are significantly improved, especially with the combination of Langmuir circulation and wave breaking effects (Figure 3.11b). This result might be explained by the non-linear interaction between wave breaking and

Langmuir circulation effects. The incorporation of all wave impacts (Epx-Allon) results in the best simulation of the upper ocean cooling among all experiments (Figure 3.11a).

To quantify contributions of different wave-related effects to the upper ocean thermal response, statistical metrics including the Mean Error (ME), Mean Absolute Error (MAE), Root Mean Square Deviation (RMSD), and Correlation Coefficient (CC) are calculated (Figure 3.13). The predominant contribution made by the combination of wave breaking and Langmuir circulation is, evidently, highlighted in the statistical metrics. Exp-WB+LC reduce ME, MAE and RMSD by ~0.36 ℃ (or ~87%) at the surface, ~70% in the upper 15 m, and over 30% beneath 18 m, compared to those of Exp-Alloff. Interestingly, the simulations including the wave breaking and Langmuir circulation separately reduce these errors (i.e., ME, MAE, and RMSD), but even the sum of their individual effects (i.e., Exp-WB and Exp-LC) are much smaller than the effect of their combination (Exp-WB+LC). This indicates the existence of non-linear effects in the combination of wave breaking and Langmuir circulation. Effects of wave breaking presents results comparable to those of Langmuir circulation, especially in the upper 10 m or so. Near the base of OML, simulations made by WB effect are slightly better than those made by LC effects. This may be attributed to the vertical momentum flux scheme by WB. Alternatively, the improvement of Stokes drift profile parameterization, e.g., estimated by the dimensional wave spectrum, may be expected to better incorporate the effect of Langmuir circulation. Coriolis Stokes force effects contribute the least, at least

in the Hurricane Arthur case, either individually or together with other wave-related processes.

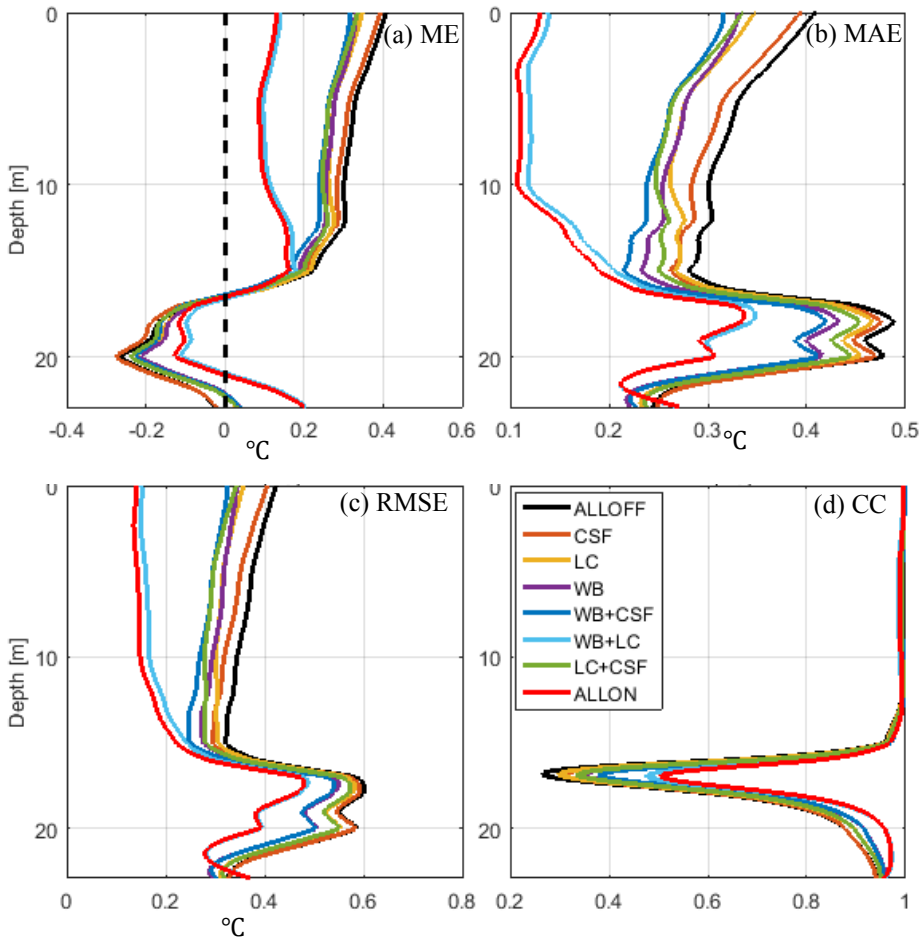

Figure 3.13: Vertical profiles of statistical metrics for simulated temperatures in eight experiments in terms of: (a) mean temperature error (ME), (b) mean absolute temperature error (MAE), (c) root mean square deviation (RMSD), (d) correlation coefficient (CC). The results are averaged over the time period from 09:00 to 21:00 UTC on July 5.

3.3.2 Wave Effects on Currents and Other Variables

In addition to thermal responses mentioned above, the storm-induced near-inertial currents are also an important feature generated by the model. Figure 3.14 shows the simulated near-inertial currents at depths 0 m, 10 m, 20 m, and 30m. Obviously, simulated current magnitudes are significantly increased due to Hurricane Arthur on 5 July and steadily decay with time after the passage of Hurricane Arthur. In the vertical, current magnitudes decay with depth. The occurrence of maximum velocity exhibits some time lags with depths, which illustrates that it takes times for the propagation of near-inertial kinetic energy from the surface to deeper layers.

The incorporation of wave-related processes (Exp-Allon), however, reveals different features. *Firstly*, wave effects reduce the simulated surface currents by over 20%, from ~1.3 m/s (Exp-Alloff) to ~1 m/s (Exp-Allon). This can be attributed to the enhanced turbulent level (Figure 3.16) in the upper ocean induced by surface wave effects. Subsequently, this results in the more homogeneous OML in comparison with the simulations without wave effects and the diminished stratification. Thus, relatively weaker currents (compared to Exp-Alloff simulation) and less shear production generated by underlying currents should be expected at the sea surface (Figure 3.15a). Illustrated by Figure 3.15a, the shear production by underlying currents in Exp-Allon is about one order of magnitude less than Exp-Alloff. *Secondly*, this less stratification in the vertical is also responsible for the lower decay rate of current magnitudes with increasing depths in OML for Exp-Allon, in comparison with Exp-Alloff. Additionally, the response time for deeper layers is shorter and the time lag is smaller in Exp-Allon than those in Exp-Alloff

(Figure 3.14). Thus, with the inclusion of wave effects, the near-inertial energy can be transported to deeper layers more efficiently rather than being trapped at the surface.

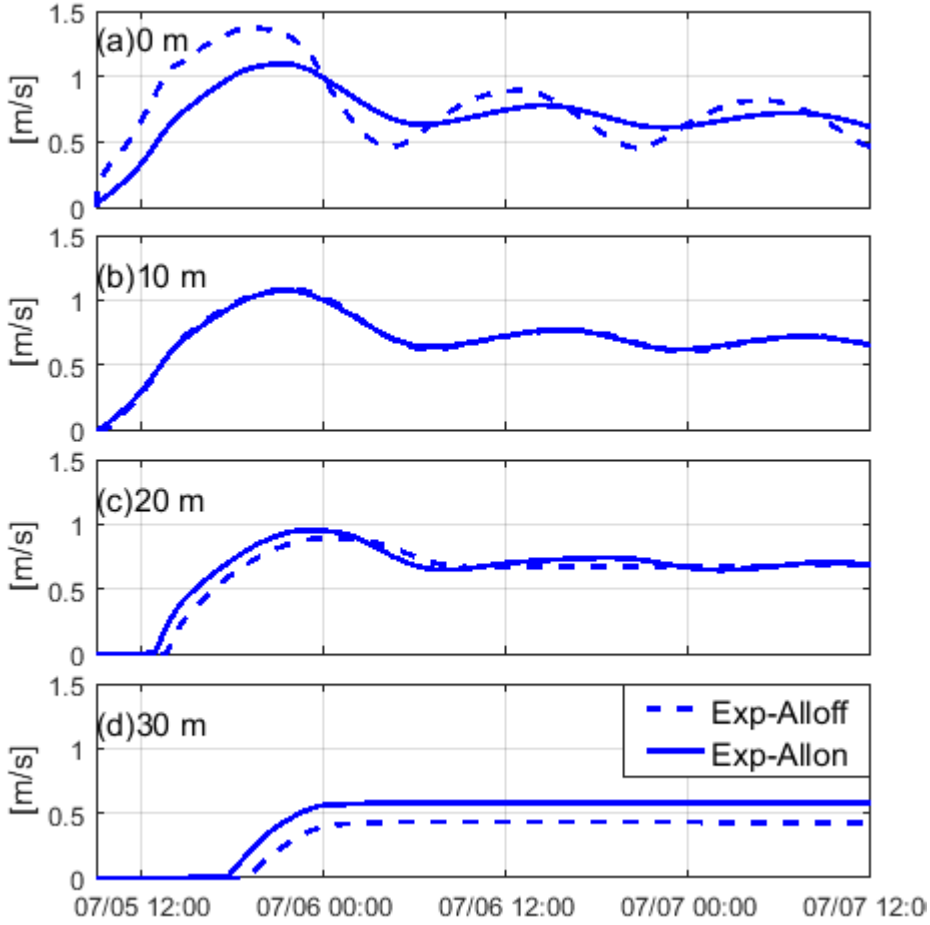

Figure 3.14: Time series of simulated current speeds in Exp-Alloff (solid line) and Exp-Allon (dash line) at depths of (a) 0 m, (b) 10 m, (c) 20 m, and (d) 30 m.

Figure 3.15 illustrates logarithmic distributions of different sources of shear production. Due to the nearly exponential decay of the Stokes drift profile [Polton et al., 2005; Li et al., 2013; Breivik et al., 2014], the magnitude of LC production decays with

depth from the surface. For simulations with LC effects, the LC shear production dominates the surface layer, presenting at least one order of magnitude larger results than the underlying current shear. With increasing depths, the role of current shear production gradually surpasses the role of LC shear, especially near the base of the OML during the hurricane forced stage (Figure 3.15), which is understandable due to the large distinction between the comparatively homogeneous OML and the thermocline water beneath.

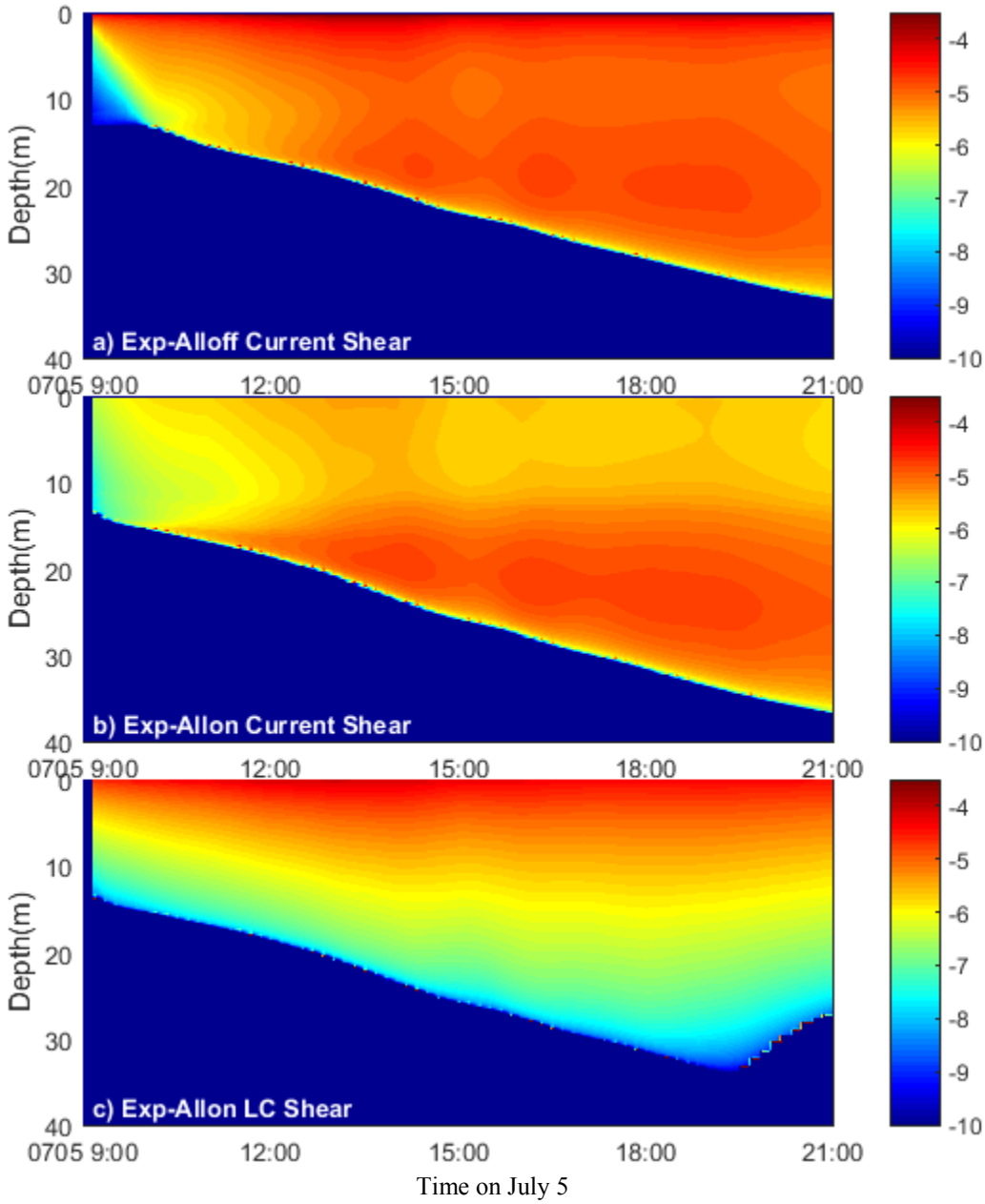

Figure 3.15: Logarithmic distributions of (a) current shear production in Exp-Alloff, (b) current shear production in Exp-Allon, (c) LC shear production in Exp-Allon with logarithmic scale colorbar. Unit: m^2/s^3.

To quantify the turbulent intensity, evolutions of TKE in eight experiments are shown in Figure 3.16. With the storm wind forcing, the simulated surface TKE notably increases up to one order in magnitude, with the TKE penetrating deeper in the vertical, compared to the previous state. Surface wave effects further extend both the magnitude and the penetration depth of TKE, especially with the contribution of LC. To quantify the important contribution of LC, the turbulent Langmuir number (hereafter La_t) suggested by McWilliams et al. [1997] is illustrated in Figure 3.17. The La_t combines the water side friction velocity and the surface value of the Stokes drift, and is primary to many parameterizations of mixing by Langmuir turbulence [e.g., Polton and Belcher, 2007; Harcourt and D'Asaro, 2008]. After 06:00 UTC July 6 when U_{10} is >15 m/s and wave age is >30, La_t, ranging from 0.25 to 0.3, is sufficiently small, which indicates that the Stokes shear can dominate the mean shear and thus the importance of Langmuir circulation [Polton and Belcher, 2007]. Before 06:00 UTC July 6 when wind speed is >15 m/s and wave ages vary 13-30, La_t ranges from 0.3 to 0.37 in a condition of high wind speeds and young-wave sea states. The importance of LC effects is illustrated by the small ratio of current shear production to the Stokes shear production (Figure 3.17) [Polton and Belcher, 2007].Without wave effects (Exp-Alloff), the maximum surface TKE induced by Hurricane Arthur is simulated as about $3\times 10^{-3}\mathrm{m}^2/\mathrm{s}^2$ (Figure 3.17), and the deepest TKE penetration (the depth at which TKE is comparable to the order of 10^{-4}) reaches about 32 m at 00:00 UTC July 6. After this time, Hurricane Arthur moved completely out of the study region, with the wind speeds declining from >20 m/s to <10 m/s. During this period both the simulated magnitude and the penetration depth of TKE

diminishes with the re-stratification of the upper ocean until 13:00 UTC on July 6 and later recovers to the previous state with small variations driven by surface winds. Wave effects intensify the TKE level of $8.2\times 10^{-3}\mathrm{m}^2/\mathrm{s}^2$, three times larger than Exp-Alloff, and deepen the penetration depth by ~20%, extending to ~38m. In Exp-Allon, the TKE level drops sharply since 00:00 UTC on July 6. However, wave effects expand the hours of high level turbulence. In Exp-Allon, the TKE takes about 16 hours to recover to the previous pre-storm level which is 4 hours longer than Exp-Alloff. Therefore, wave effects, not only enlarge the magnitude and the penetration depth of TKE, but also extend the time for the high TKE level to endure. Of these wave-related processes, the inclusion of Langmuir circulation makes the most remarkable contribution.

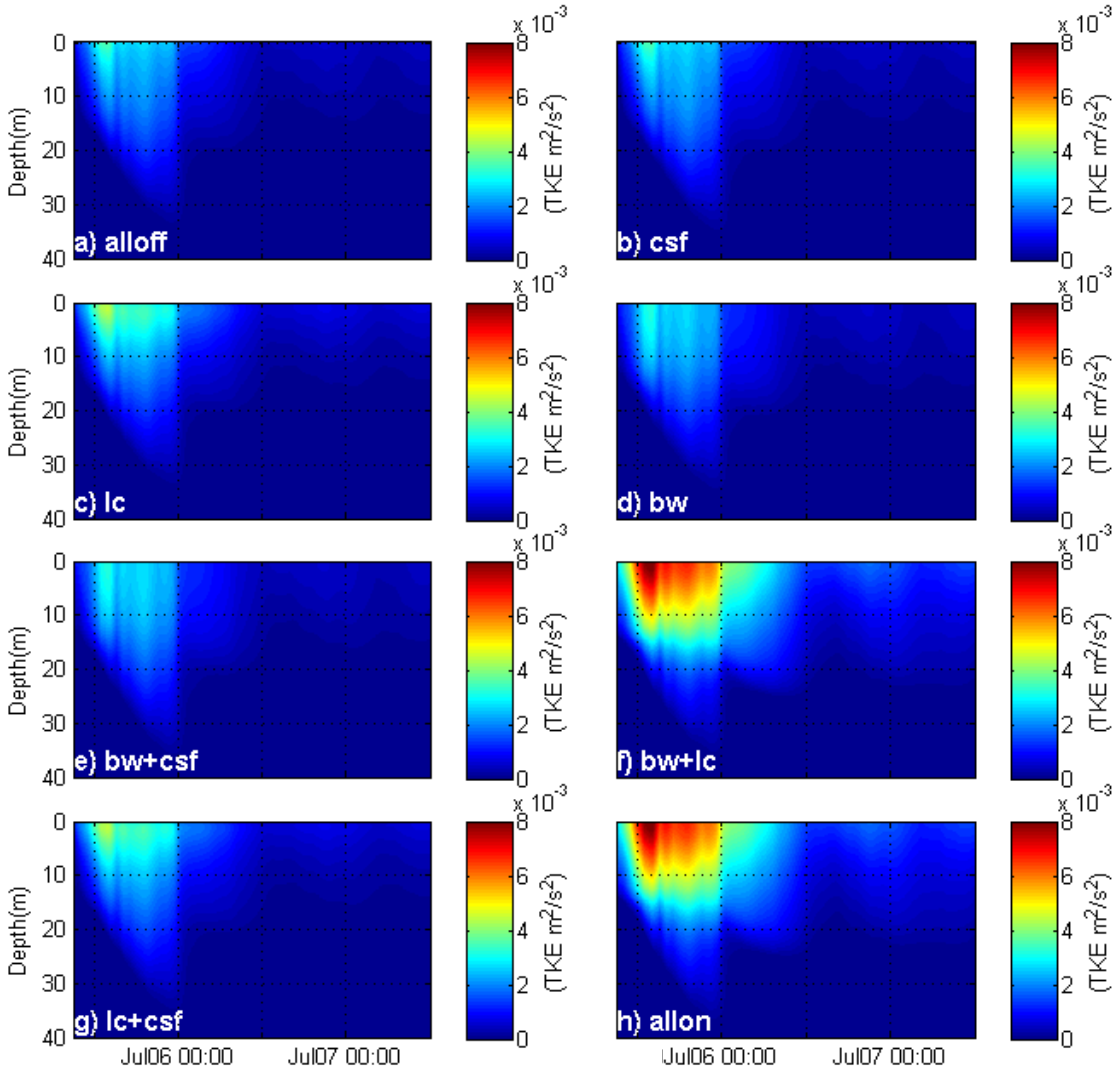

Figure 3.16: Time-depth distributions of simulated turbulent kinetic energy (TKE) transport for cases of: (a) Exp-Alloff (no wave effects), (b) Exp-CSF (only influence of CSF), (c) Exp-LC (only influence of LC), (d) Exp-WB (only influence of wave breaking), (e) Exp-WB+CSF (influences of CSF and wave breaking), (f) Exp-WB+LC (influences of LC and wave breaking), (g) Exp-LC+CSF (influences of CSF and LC), (h) Exp-Allon (all wave effects).

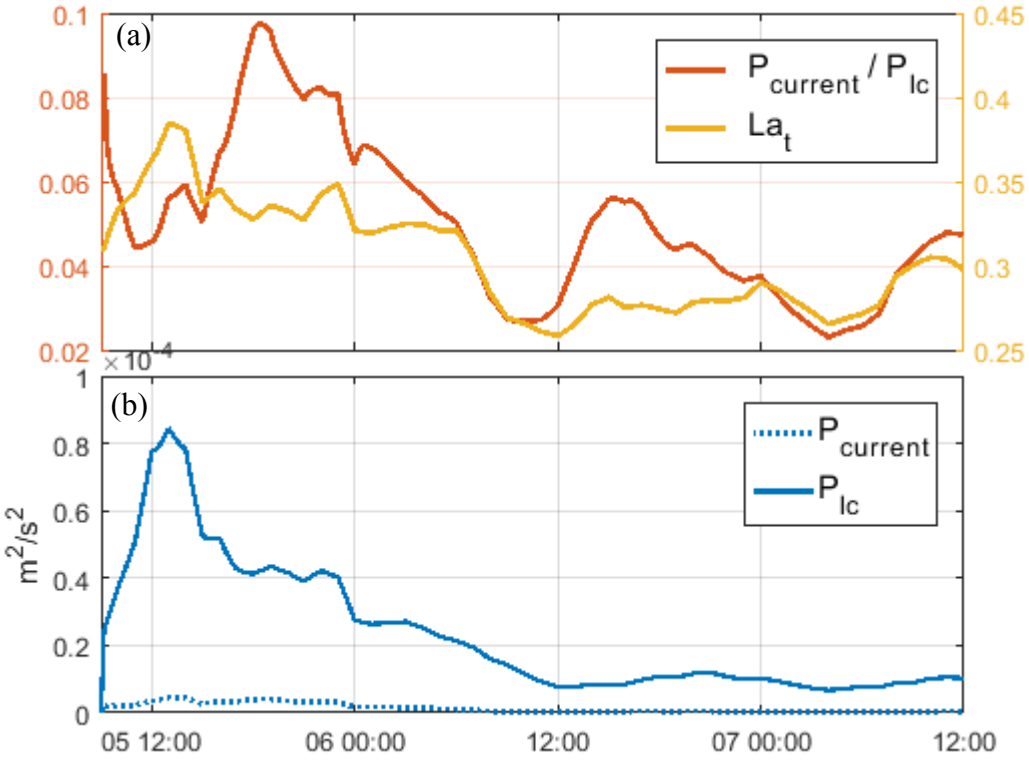

Figure 3.17: Time series of turbulent Langmuir number (yellow), surface shear production by currents (dashed blue) and by Langmuir circulation (solid blue) of Exp-Allon, and the ratio of mean-flow shear production versus LC shear production (red).

3.4 Sensitivity Experiments

As discussed in Zedler et al. [2002], 1D simulations of ocean responses to storms are sensitive to the surface wind stress. The parameterization of wind stress, specifically the drag coefficient in the bulk formula, is currently of controversial, especially for extreme wind conditions such as hurricane winds. Hsu et al. [2007] gave a general overview of previous parameterizations of the drag coefficient in tropical cyclone wind conditions. Many studies suggested that there is an evidently linear relation between drag coefficients (C_d) and wind speeds (U_{10}) for moderate winds [e.g., Large and Pond, 1981; Edson et al. 2013]. In addition, C_d is also shown to have dependency on the sea state (e.g., surface roughness, surface wave height, and wave age) [Donelan et al., 2004; Holthuijsen et al., 2012]. The parameterizations of C_d under extreme wind conditions have been studied extensively using atmospheric and oceanic measurements [e.g., Powell et al. 2003; Black et al. 2007; Jarosz et al. 2007; Sanford et al. 2011], laboratory experiments [e.g., Donelan et al., 2004], and model simulations [e.g., Chen et al., 2013]. There are a large number of drag coefficient parameterizations, some of which, however, are not appropriate to our cases. In particulate, the bulk algorithm 3.0 [Fairall et al. 2003] developed from the Coupled Ocean-Atmosphere Response Experiment (COARE) lacks the comprehensive information for high-wind conditions. For instance, the Charnock parameter has to be set as constant for winds larger than 18 m/s due to the deficiency of observations beyond this wind speed at that time. Based on COARE3.5 [Edson et al. 2013], C_d is parameterized based on the observations including high-wind measurements, but the high-wind observations were mostly under fully-developed sea states. Our model simulations,

however, focus on the storm forcing at the forced stage, at which most of the waves are very young. Donelan et al. [2012] took the wave age into account, but it was based on laboratory experiments which might differ from realistic ocean conditions. Their estimations of C_d are smaller than most of other parameterizations, especially for winds <26 m/s.

In our model simulations, the drag coefficient is parameterized as a combination of Large and Pond [1981] for low and moderate winds and Powell et al. [2003] for high winds (Equation 3-1), which has been used in previous hurricane studies [e.g., Oey et al., 2006]. To determine how large the impact of momentum forcing with different parameterizations of the drag coefficient on model simulations of upper ocean responses could be, we choose another three drag coefficients (Table 3.8), i.e. Large and Pond [1981], Black et al. [2007], and Zijlema et al. [2012], to estimate wind stresses and force the model. Large and Pond [1981] reported that C_d is a constant for low winds ($|U_{10}| \leq$ 11m/s) and increases linearly with moderate wind speeds (11m/s $\leq$ $|U_{10}| \leq$25m/s). Black et al. [2007] suggested a parameterization for C_d by synthesizing a collection of high-wind air-sea transfer observation experiments. Zijlema et al. [2012] established an alternative wind drag parameterization by using a weighted second order polynomial to curve-fit a large numbers of comparatively recent observation data sets. Wind stresses estimated with these three parameterizations for C_d are used in this study to force the newly-modified GOTM with the same model settings in Exp-Alloff and Exp-Allon.

$$C_d \times 10^3 = \begin{cases} 1.2, & U_{10} \le 11\, m/s \\ 0.49 + 0.065\, U_{10}, & 11 < U_{10} \le 19 m/s \\ 1.364 + 0.0234 U_{10} - 0.0002 {U_{10}}^2, & 19 < U_{10} \le 100 m/s \end{cases} \quad (3\text{-}1)$$

The storm-induced temperature change profiles for sensitivity experiments and related statistical indices [Moriasi et al., 2007] are shown in Figure 3.18 and Table 3.9. Sensitivity experiments support previous results [e.g., Zedler et al. 2002] that the 1D simulation of ocean responses to storms is indeed sensitive to surface wind forcing. The sensitivity experiments also demonstrate that the surface wave effects on improving model simulations. In general, the reference simulation Exp-Allon with C_d of Large and Pond [1981] and Powell et al. [2003] gives the best simulation with the smallest root-mean-square error (RMSE), mean error (ME), and mean absolute error (MAE), and the highest correlation coefficient (CC) among these four experiments. The RMSE-observations standard deviation ratio (RSR) suggested by Moriasi et al. [2007] is a relative indicator of RMSE normalized by observed standard deviation, which describes the relative discrepancy of simulations from observations. All the RSRs are less than 0.7 [Moriasi et al., 2007], which indicates all model results of sensitivity experiments commonly give reasonable simulations, though simulations change with different parameterizations of C_d. Figure 3.18a-b show that simulation biases are generally larger near the base of the OML than those of the top 17 m for all these four experiments. Different forcing conditions change temperature responses with slight underestimations for the upper ocean cooling in Exp-C_{d1} and small overestimation in Exp-C_{d2} and Exp-C_{d3}. With the incorporation of wave effects, both the mean RMSE and RSR are reduced

from ~0.50 to ~0.14, and the mean CC is increased from 0.97 to 0.99. Significant improvements can also be detected in Figure 3.18. These improvements suggest that though the simulations are sensitive to wind stress, the simulations with surface wave effects agree better with the glider observations than those without wave effects.

Table 3.8: Sensitivity experimental design on drag coefficients

	C_{dREF}	C_{d1}	C_{d2}	C_{d3}
Methods	Large & Pond [1981] Powell et al. [2003]	Black et al. [2007]	Large & Pond [1981]	Zijlema et al. [2012]

Table 3.9: Root mean square errors (RMSE), RMSE-observations standard deviation ratio (RSR), and correlation coefficients (CC) for the temperature difference between 09:00 and 14:00 UTC on July 5, 2014 for the top 25 m water.

	Large&Pond Powell	Black et al. [2007]	Large & Pond [1981]	Zijlema et al. [2012]	Average
RMSE_OFF	0.472	0.589	0.411	0.366	0.459
RMSE_ON	0.089	0.231	0.094	0.128	0.135
RSR_OFF	0.513	0.641	0.447	0.398	0.499
RSR_ON	0.097	0.251	0.102	0.139	0.147
CC_OFF	0.894	0.809	0.927	0.946	0.973
CC_ON	0.998	0.981	0.995	0.991	0.995

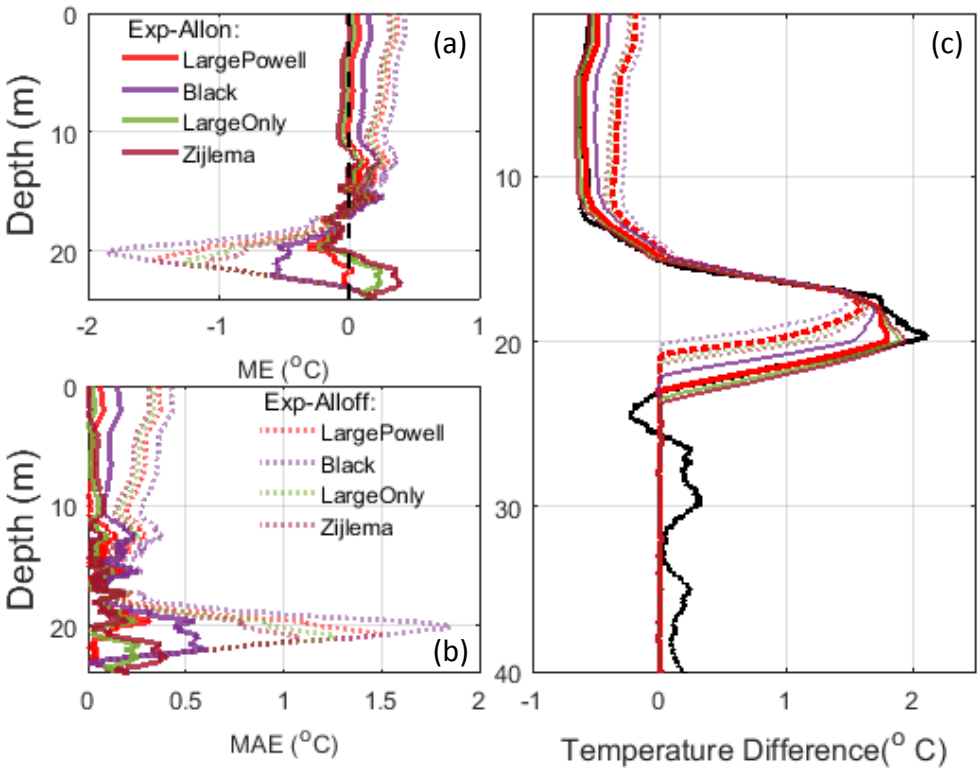

Figure 3.18: (a) Wind stress time series used for sensitivity experiments to force the GOTM model using the drag coefficients suggested by Oey et al. [2006], Black et al. [2007], Large and Pond [1981] and Zijlema et al. [2012]. (b)Simulated (color curves) and measured (black curve) profiles of storm-induced temperature changes in the upper 40 m for the four wind stress forcing cases indicated in (a). The dash curves denote simulated temperature difference Exp-Alloff, and solid curves denote those of Exp-Allon. The temperature difference profile was computed from the temperature profile at 14:00 UTC subtracting 09:00 UTC on July 5 2014.

Chapter 4

Wave Effects on Ocean Responses to Hurricane Felix

In the previous chapter, the surface wave effects on the upper ocean thermal responses to Hurricane Arthur were evaluated based on glider observations and model simulations. It should be noted that the ocean current responses were not validated due to the lack of the measurements of ocean currents. Different from glider observations during Hurricane Arthur, ocean currents were observed at the Bermuda Testbed Mooring (BTM) site, which show strong storm-induced currents, along with the oceanographic and meteorological conditions, during the passage of Hurricane Felix (1995). The prestigious mooring observations with other *in situ* observations allow us to study another important hurricane-induced feature, the near-inertial currents (NIC). In this chapter, the newly-modified 1D depth-dependent GOTM model is applied to Hurricane Felix. The main objective of this chapter is to examine the surface wave effects on the upper ocean responses to Hurricane Felix over the open ocean of the northwest Atlantic.

We discussed the justifications for using 1D model in Hurricane Arthur case in section 3.2.1. The same justifications are applicable to Hurricane Felix. On August 15, the eyewall (northeast sector) of Hurricane Felix passed almost directly over the BTM site

with the averaged translation speed of ~6.7 m/s, which was a relatively fast-moving hurricane. Dickey et al. [1998] conducted a scale analysis suggested by Price et al. [1994] and demonstrated that the upper ocean responses to Hurricane Felix presented a first order of one-dimensional response. For instance, the Burger number [Price et al., 1994] of Hurricane Felix is relatively small, which indicates the nonlocal dynamics of the relaxation phase were not as important during forced stage. The mixed layer Rossby number [Price et al., 1994] indicates that nonlocal or advective effects were likely not important during the forcing and early decay stages (the first several days of the e-folding time scale).

Based on these justifications, Zedler et al. [2002] conducted 1D depth-dependent simulations with four turbulence schemes and suggested that the observed temperature and current responses can be partially explained. It is reasonable that 1D models cannot be expected to resolve all features of observed responses due to the nature of three-dimensional processes, e.g. internal gravity waves and inertial pumping. However, these models do not explicitly include all the 1D-related processes, e.g. effects of surface gravity waves which have been proven to have undeniable impacts on upper ocean mixing processes. Thus, simulations of upper ocean responses to Hurricane Felix with surface wave effects by our newly-modified GOTM are presented in this chapter.

4.1 Overview of Observed Ocean Conditions during Hurricane Felix

Based on the AVHRR satellite image of SST [Nelson, 1996], the eyewall (northeast sector) of Hurricane Felix passed almost directly over the BTM site, with the hurricane

eye center only ~65 km away from the BTM site. The BTM site, located at ~80 km southeast of Bermuda, was used to collect high temporal resolution, long-term data, including meteorological measurements at the surface and subsurface measurements of currents, temperature, conductivity, etc (http://www.opl.ucsb.edu/html-old/btm.html). These data recorded oceanic conditions during the passage of Hurricane Felix. These measurements were taken by multivariable moored systems (MVMS) and S4 current meters [Dickey et al., 1998] at depths of 25, 44, 65, and 71 m. The temporal resolutions are on a scale of minutes.

The vertical resolutions of BTM data, however, are too coarse to precisely resolve the upper ocean thermal structures. Thus, high vertical resolution data sets at two other sampling sites nearby are used as supplementary data sets to describe ocean conditions before and after Hurricane Felix. One site is the Bermuda Atlantic Time-series Study (BATS) of the U.S. Joint Global Ocean Flux Study (JGOFS) program, located less than 12 km south of the BTM site, which collected monthly measurements (http://batsftp.bios.edu/). The other site is the world's first significant deep-ocean time series, Hydrostation S (http://batsftp.bios.edu/Hydrostation_S/), located ~73 km northwest of the BTM site, which collected bi-weekly measurements [Figure 1a, Zedler et al., 2002]. These oceanographic observations at these sites are valuable for the study of storm-induced modifications of oceanic conditions (both the temperature field and the ocean current field) during Hurricane Felix. More information of these data sets is shown in Table 4.1.

Table 4.1: List of available data sources during Hurricane Felix (1995)

Data source	Time Period	Variables	Depths	Reference
BTM	August 1-23	U_{10}, T_{air}, Temperature	Surface	Dickey et al., [1998]
		Temperature	25, 44, 65, 71m	
		Currents	25, 44, 71 m	
Hydrostation S	August 10	Temperature, Salinity	7 - 2604.2 m	Michaels and Knap [1996]
BATS	August 18	Temperature, Salinity	6 - 504 m	Steinberg et al., [2001]
			6 - 4206 m	
Buoy 41001	August 1-23	Meteorology	Surface	NDBC

4.1.1 Thermal Conditions and Responses

Before the passage of Hurricane Felix, typical summer stratification of the upper ocean occurred at the BTM site, with a <25 m seasonally warmed surface mixed layer (~28 ℃) over the thermocline. The surface mixed layer temperature gradually increased from ~23 to ~28 ℃ since mid-July (Figure 4.4), with the statistically significant slope of 1.2 ℃/week. Consequently, the stratification of the upper ocean occurred with a positive trend (Figure 4.4). Michaels and Knap [1996] suggested that there were small spatial differences in temperature and salinity structures over the vicinity of BTM site. They quantified that the temperature differences at any given depth in the main thermocline between BATS and Hydrostation S are <1.2 °C in spring and summer. Their suggestion is supported by the 3-day composite AVHRR satellite images which illustrated the approximately uniform (29 $\pm$0.5) SST in the horizontal direction (Figure 4.1). Figure 4.4

shows that measurements at BTM at depths 25 m, 44 m and 60 m are consistent to the temperature profile measurements at Hydrostation S site on August 10 and those at BATS site on August 18, respectively.

After the passage of Hurricane Felix, 3-day composite satellite image (August 16-18) illustrates the regional pattern of the storm-induced SST cooling (Figure 4.1b). SST was observed to decrease roughly from ~28.5 ℃ to ~25.5 ℃ over a large swath of nearly 350 km width. The largest SST cooling reached 3.8 ℃ and occurred southwest of Bermuda, in the vicinity of the BTM location [Nelson, 1996]. It is interesting to note that the BTM was located in the center of Hurricane Felix's wake which was about 200 km to the right of the hurricane eye (looking in the direction of the hurricane's motion) [Dickey et al, 1998], based on sections of SST along 31.75°N (Figure 4.2). In the vertical direction, the cooling of the upper ocean mixed layer and the heating beneath the OML were easily detected in Figure 4.4, e.g., the 25-m temperature reduced by 3.5-4 ℃ and the 44-m, 65-m increased by ~2 ℃, ~1 ℃ respectively. It is also found that increasing trends of water temperature and vertical stratification of the upper ocean were interrupted by Hurricane Felix (Figure 4.4) on August 15. Moreover, Figure 4.4 also suggests that the vertical stratification of the upper ocean was significantly decreased. The OML was remarkably deepened by at least 20 m (from ~25 m to >44 m) at the BTM and was deepened to ~47 m at the BATS site. Restoration of the upper ocean to pre-hurricane conditions occurred on the order of 10 days [Nelson, 1998]. These effects indeed had undeniable impacts on subsequent hurricanes that travelled over the wake of Hurricane Felix and the following seasonal heat budget for the Bermuda region.

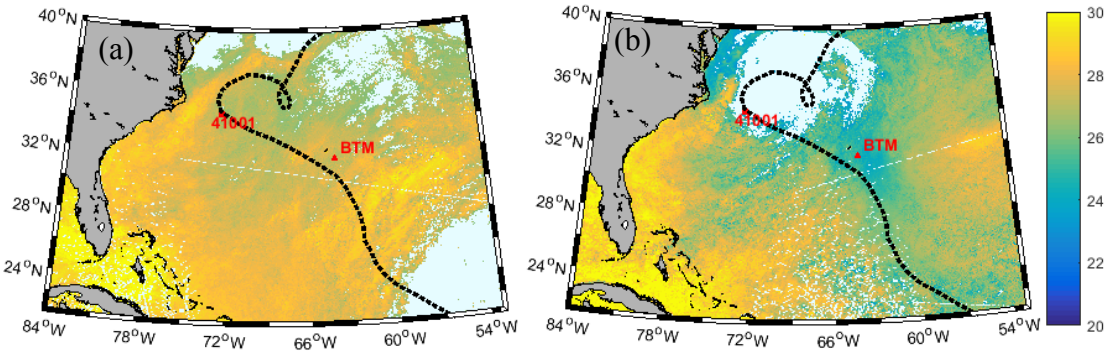

Figure 4.1: AVHRR three-day composite SST images for the period of (a) August 11-13 1995 before Hurricane Felix and (b) August 16-18 1995 after Hurricane Felix. The black dash line denotes the track of Hurricane Felix with the Best Track Data of Atlantic Hurricane Database (http://www.nhc.noaa.gov/data/#hurdat). Red triangles indicate locations of Bermuda Testbed Mooring site and buoy station 41001 used for validation.

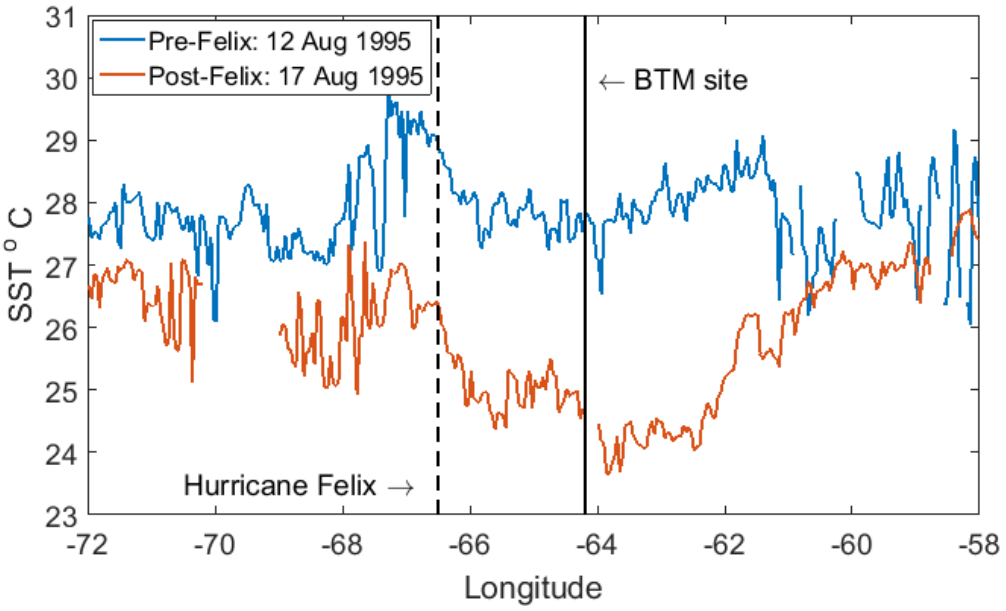

Figure 4.2: Sections of SST along the latitude of BTM (31.75°N) from 3-day composite AVHRR images, centered on August 13 (blue) and August 17, 1995 (red). The black dash line indicates the longitude of Hurricane Felix when it passed by the latitude of 31.75°N, the black solid line is that of the BTM site.

4.1.2 Current Fields and Responses

Prior to the passage of Hurricane Felix, the sea surface wind speeds (U_{10}) at BTM were less than 14 m/s and significantly increased to ~30 m/s on August 14 (Figure 4.3). During hurricane's forced stage, strong currents were observed in the OML and thermocline, with the maximum observed ocean currents up to ~1.2 m/s at the depth of 25 m. Significant near-inertial motions were detected at depths of 25 m and 44 m (Figure 4.5). Evidently, the u-components (eastward) and v-components (northward) are $\pi/2$ out of phase with v-component leading, which indicate a clockwise near-inertial motion. These intense near-inertial currents (hereafter NIC) are of the special interest due to their important role in the vertical propagation of energy to the ocean interior and the shear-instability induced turbulence near the base of the OML. There were no significant NICs at the depth of 71 m, which could possibly be explained by the inertial beating which is described as the out-of-phase between the first internal gravity wave mode and higher modes [Qi et al., 1995; Zedler et al, 2002].

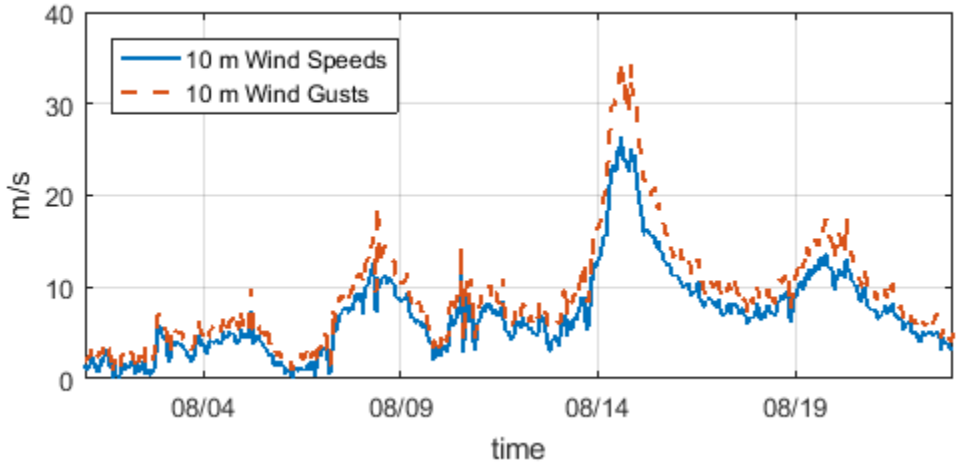

Figure 4.3: Time series of observed wind speeds (solid blue curve) and wind gusts (dash blue curve) at 10 m above the sea surface at the BTM site.

Generally, the ocean currents at 25 m and 44 m show a large percentage of energy near the local inertial frequency of 0.0440 cph, or the local inertial period of 22.8 hours, after the passage of Hurricane Felix. In order to further examine the near-inertial component of currents, we use the rotary spectral analysis to identify the dominant frequency of all BTM current time series, based on the methodology suggested by O'Brien and Pillsbury [1974]. Rotary spectra analysis is a useful technique that separates vector time series (e.g., currents or winds) into clockwise and counter-clockwise rotating components. In this case, since the near-inertial components rotate clockwise in the North Hemisphere, the power spectral density distribution is indicated by the negatively (clockwisely) rotating power spectrum. The dominant frequency of BTM currents is ~0.0469 cph (or dominant period of 21.3 hours), ~6% higher than the local inertial frequency, which is termed as the blue shift. The dominant frequency of current (or

temperature) oscillations in the thermocline shifts about 1 to 5% higher than the local inertial frequency. The amount of the frequency-shift is usually proportional to one half the mixed-layer Burger number. This phenomenon is considered as a measure of the pressure coupling between the mixed-layer and thermocline currents [e.g., Price, 1983; Price et al., 1994; Church et al., 1989; Shay et al., 1998]. Price [1983] applied the blue shift parameter ($\nu = (\omega - f)/f$, where ω is the observed dominant frequency) as an important indicator denoting the vertical propagation angles for near-inertial wave rays towards the deep ocean. This near-inertial frequency, ~0.0469 cph, is also detected for temperature time series at depths of 71 m, 60 m, 44 m and 25 m, which indicates temperature oscillations induced by internal gravity waves near the inertial period. This large-amplitude oscillation of temperature is especially remarkable at depths around 60 m and 70 m with temperature fluctuating ~1.5℃ (Figure 4.4). This effect is denoted as inertial pumping and Dickey et al. [1998] estimated the vertical amplitudes of the waves as roughly 15 m.

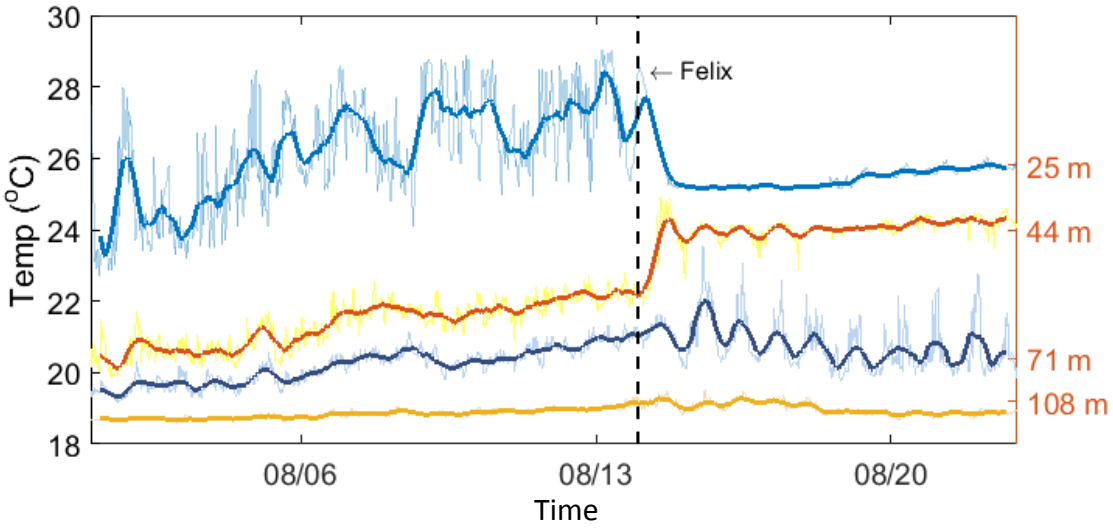

Figure 4.4: Time series of observed temperature at depths of 25, 44, 71 and 108 m at the BTM site with temporal resolutions of 30 min, 3.75 min, 3.75 min, and 30 min, respectively. The thick curves indicate time series of 12-hour filtered temperature to emphasize the temperature initial-oscillation at depths of 44-71 m.

To further quantify the intensity of inertial currents, the band-pass filter is applied to the time series of observed ocean currents with the passband near the dominant frequency. This approach allows the separation of the near-inertial component from total currents. The amplitudes of observed NIC at different sampling depths are obtained. Within the mixed layer, the NICs were almost instantaneously generated by Hurricane Felix with the maximum amplitude up to ~60 cm/s at the depth of 25 m (Figure 4.5a), which explains 87% of the total currents. Subsequently, the amplitude of NIC steadily decays with the e-folding decay time of 14.9 days. The slightly increasing fluctuation on August 20 is likely induced by a strong wind event on the preceding days. At the depth of 44 m, the amplitude of NIC dramatically increased to ~45 cm/s at the end of August 15, but reached a maximum of ~50 cm/s on August 17 (Figure 4.5b). This phenomenon is

likely attributed to the coupling of hurricane-induced inertial currents and the add-on of inertial energy transported from the upper layers. The e-folding decay period of 44 m is estimated to be roughly 5.2 days, which is roughly two times higher than that at 25 m. This result is understandable, since the decaying processes, such as strong shear-instabilities induced turbulence [Crawford and Large 1996; Skyllingstad et al. 2000] and the radiation of energy by internal gravity waves [Price, 1983; D'Asaro et al., 1995], are more vigorous near the base of the mixed layer than within the mixed layer.

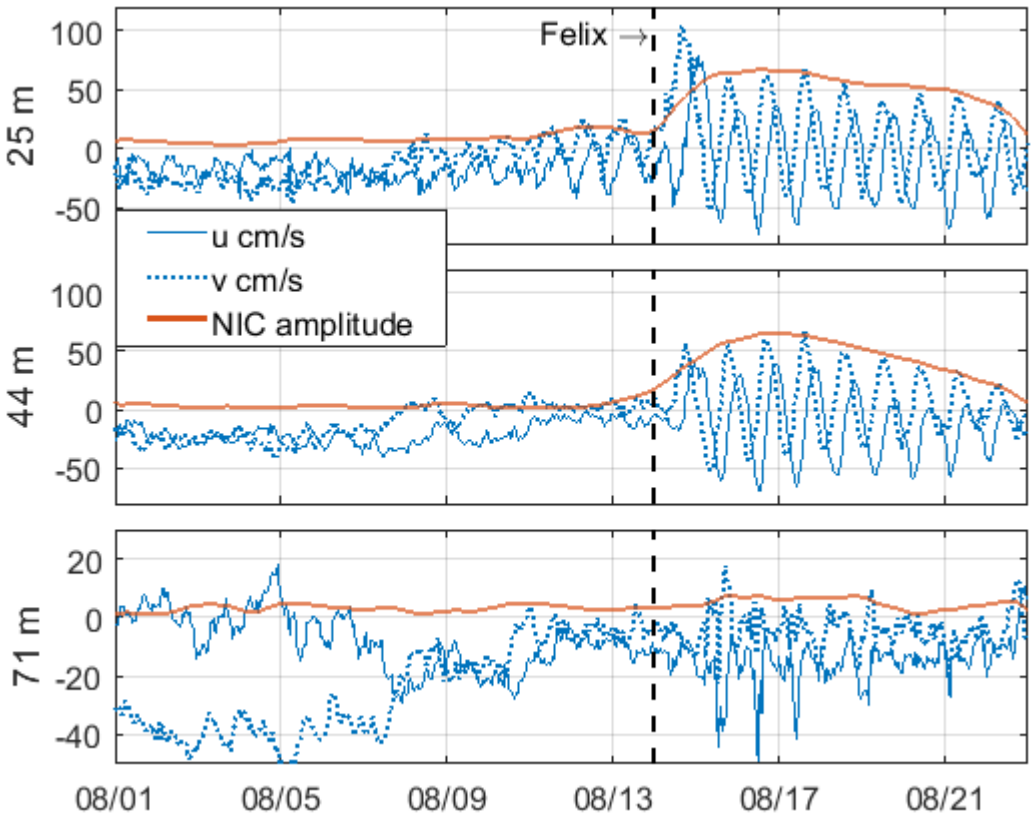

Figure 4.5: Time series of observed currents at depths of 25, 44, and 71 m at the BTM site with the solid blue denoting eastward component and dashed blue northward component. The thick red curves indicate time series of near-initial amplitudes by a band-pass filter with the passband ranging 0.8-1.2 f.

4.2 1D Circulation Model, Model Initialization and Surface Forcing

In this section, the modified 1D GOTM model, particularly the model initialization and the forcing conditions are introduced. This 1D model is a depth-dependent model for studying ocean hydrodynamic processes related to vertical mixing with the neglection of the lateral gradients and advection terms. In this study, GOTM is modified by including wave-related processes, i.e., wave breaking, Langmuir circulation and Coriolis-Stokes force, with the consideration of wave age effects. In the next sections, more information of initialization and forcing conditions are specified.

4.2.1 Initialization

To examine the upper ocean responses to Hurricane Felix, numerical simulations start on August 13 1995 as close as possible to the approach of Hurricane Felix. Since the vertical resolution of observations at the BTM site was too coarse to comprehensively resolve the thermal structure within the thermocline, high resolution profiles are required for initializing numerical model simulations. Michaels and Knap [1996] suggested that there was small spatial difference in the vertical temperature structure between the BTM site and a nearby observation station known as Hydrostation S that provides biweekly high-resolution temperature profile measurements. Measurements at Hydrostation S closest to Hurricane Felix were only available on August 10. Zedler et al. [2002] argued that the variation of BTM temperature between August 10 and 13 1995 was small (several tenths of a degree) so that the Hydrostation S temperature profile on August 10 was used as the profile of August 13 to initialize their 1D simulations. Based on satellite

remote sensing data, the pre-storm SSTs on August 10 at Hydrostation S and BTM measurements (Figure 4.1) were indeed similar to each other. In Figure 4.6, the temperature structure of the upper ocean (< 25 m) also had a slightly difference between August 10 and August 13. Thus, the temperature profile of the upper ocean (< 25 m, or above the OML) at the Hydrostation S site on August 10 was used to initialize the model simulation. By comparison, the temperature structure below the surface mixed layer and within the thermocline had significant differences between August 10 and August 13, with the maximum up to 1℃. We thus modified the temperature profile at Hydrostation S on August 10 below the mixed layer based on measurements at BTM on August 13 by curve fitting. The newly-modified temperature profile was then set to be the initial condition in simulations of ocean responses to Hurricane Felix.

For the initial condition of salinity, there was little difference between the simulation initialized with observed salinity profiles and that with constant salinity. As a result, the salinity profile at Hydrostation S on August 10 is used as the initial salinity condition for simulation.

For the initial condition of ocean current fields, the amplitude of observed NIC was up to ~20 cm/s on August 13 at the depth of 25 m, which might have interacted with hurricane-generated NIC. Unfortunately, we were not able to initialize ocean current fields with observed currents, since the only three depths of current data were available which are too coarse to resolve the vertical structure of currents. Thus, we set the initial currents to be zero.

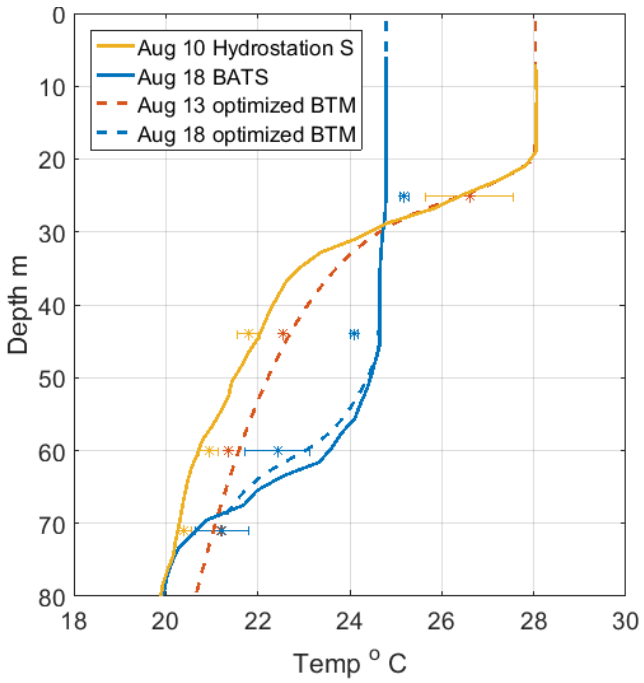

Figure 4.6: Vertical profiles of observed (solid) temperature on August 10 at Hydrostation S (yellow) and August 18 1995 at BATS site (blue). Asterisks denote observed temperatures at certain depths at the BTM site on August 10 (yellow), 13 (red) and 18 (blue) 1995. The error bars are ± 1 standard deviation from the mean. Dashed curves are the BTM temperature profiles optimized by BTM observations based on observed profiles in the other two sites.

4.2.2 Forcing Conditions

The wind speeds used to force the 1D model were measured at 4.2 m above the sea surface from a buoy tower at the BTM site. The observed wind speeds were adjusted to standard wind speeds at 10 m above the mean sea surface following Hsu et al. [1994]. Wind stresses were calculated using the bulk formula, with the drag coefficient taken from Oey et al. [2006] (Equation 3-1). This high-wind-limited drag coefficient curve fits the low-to-moderate wind measurements following the method of Large and Pond [1981]

and high tropical-cyclone wind measurements following the method of Powell et al. [2003].

The heat flux was calculated through the method of COARE 2.5 [Fairall et al., 1996], with the use of observed sea surface air temperature, sea surface temperature from BTM measurements, and air pressure, cloud cover and relative humidity from CFSR. Due to the lack of SST no measurements at the BTM site, temperatures at 25 m are used as substitutions for the following reasons: (a) the depth of 25 m was near the base of pre-storm OML and was completely within the post-storm OML, (b) the temperatures within the OML is typically quasi-homogeneous, and (c) the temperatures at the depth of 25 m were similar to the satellite remote sensing SST. The same substitution was also used by Zedler et al. [2002]. This is likely to introduce small errors, particularly prior to the passage of Hurricane Felix, since 25 m was located near the base of the pre-storm surface OML. But these errors reduce with the arrival of Hurricane Felix, since the surface mixed layer was rapidly deepened to 46 m. By that time, 25 m temperatures should be relatively good representations of SSTs due to the nearly homogeneous hydrography within the mixed layer.

Due to the lack of wave measurements, wave conditions are specified by model outputs of WAVEWATCHIII (WW3, ftp://ftp.ifremer.fr/ifremer/ww3/HINDCAST/). The WW3 outputs were validated by buoy measurements at station 41001 with respects to significant wave heights and peak wave periods (Figure 4.7). Though the Stokes drift velocity profile is important in estimating the shear production of Langmuir circulation

and the Coriolis-Stokes force, no wave spectrum measurements are available for Stokes profile validation.

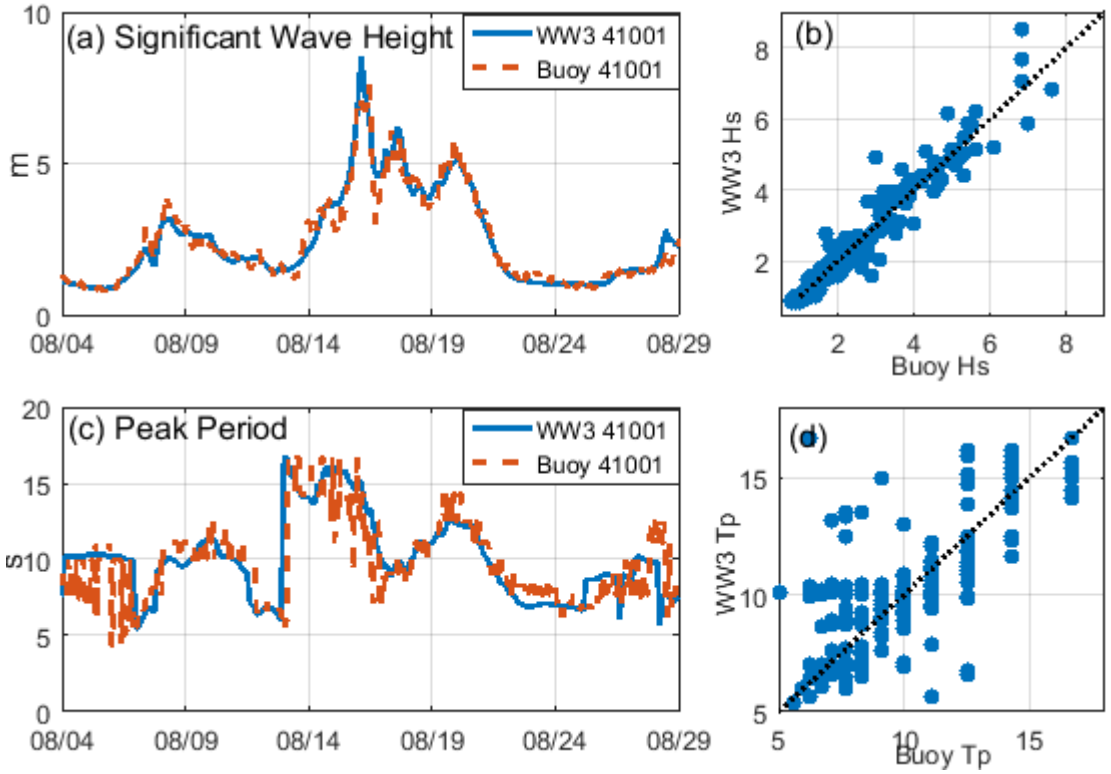

Figure 4.7: Time series of observed (red dashed line) significant wave heights (upper panel) and peak wave periods (lower panel) in comparison with WAVEWATCH III (blue solid line) at buoys 41001 during the passage of Hurricane Felix (August 14-29, 1995).

Table 4.2: Root mean square error (RMSE) and correlation coefficient (CC) for the significant wave height (H_s) and the peak wave period (T_p) with confidence level > 99%.

Buoy	RMSE_H_s (m)	CC_H_s	RMSE_T_p (s)	CC_T_p
41001	0.32	0.98	1.94	0.71

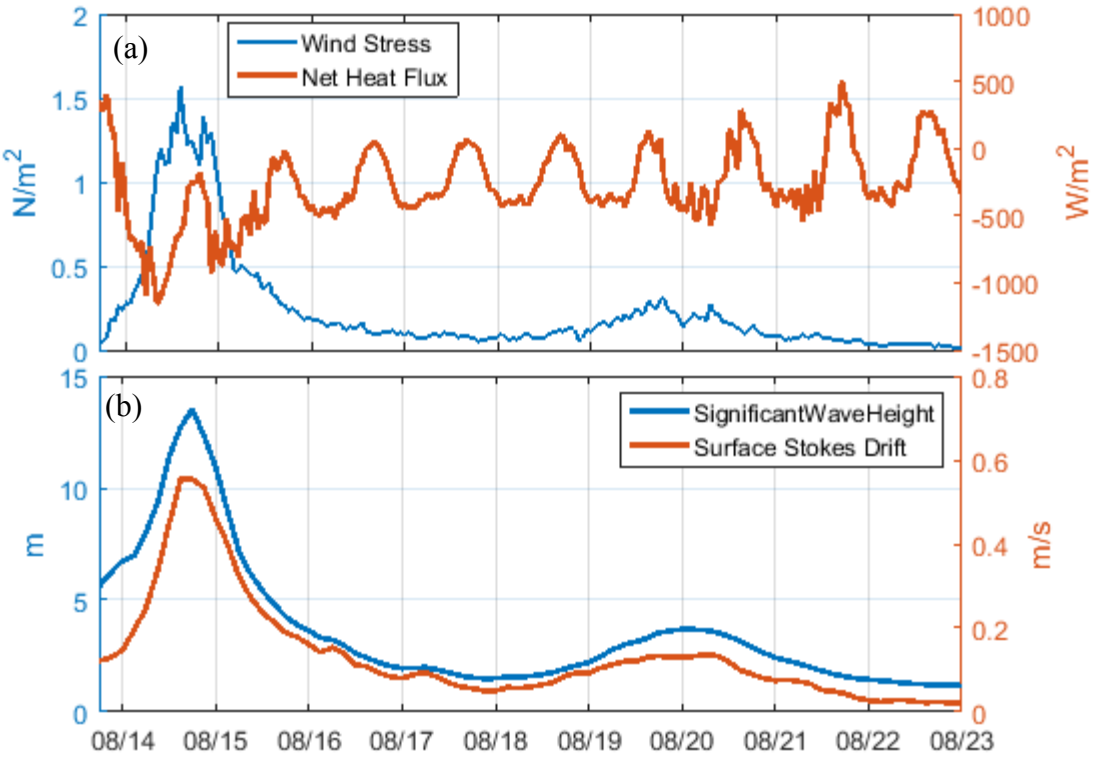

Figure 4.8: Time series of (a) wind stresses and net heat flux, (b) significant wave heights and surface Stokes drifts at the BTM site from 16:00 on August 13 to 00:00 on August 23, 1995. The wind stresses are calculated using the drag coefficient suggested by Large and Pond [1981] and Powell et al. [2003].

4.3 Model Results

In this section, the newly-modified GOTM with surface gravity wave effects is applied to Hurricane Felix. The impacts of surface waves on both the thermal structure and the inertial motion responding to hurricanes are examined based on the numerical simulations and the observations. Since the results of thermal responses are similar to the Hurricane Arthur case, we focus mainly on the wave effects on NIC in the following sections.

4.3.1 Simulated Thermal Responses

We apply the newly-modified 1D GOTM for simulations of upper-ocean responses to Hurricane Felix with variant combinations of wave-related effects. With the incorporation of wave effects, simulated SST cooling extends from 2.5 ℃ to 3.2 ℃, and OML, defined as the depth where temperature is 1 ℃ less than SST [Lamb et al., 1984; Wagner et al., 1996], deepens from ~36 m to ~46 m (Figure 4.9). The temperature profile modification by Hurricane Felix demonstrates that both the hurricane-induced upper-ocean cooling and heat-pump to subsurface depths are enhanced by surface gravity wave effects. The Exp-Allon simulation versus the non-wave (Exp-Alloff) simulation strengthens upper ocean cooling by 0.7 ℃ (~22% of total observed cooling), with OML increased by 10 m (~50% of observed OML deepening due to Hurricane Felix). Coupled atmosphere-ocean models demonstrate that even small shifts in sea surface temperature and stratification even on small (100km) horizontal scales, can have significant impacts on storm intensity [Glenn et al., 2016]. Same as the Hurricane Arthur case, the simulation

of Exp-Allon achieves the better agreement with the observed storm-induced temperature changes than other model runs (Figure 4.9). The contribution of wave-related processes at the hurricane forcing stage has been discussed in the simulation of Hurricane Arthur. For Hurricane Felix, we are not able to discuss it because of the lack of the temperature profile observations at the forcing stage.

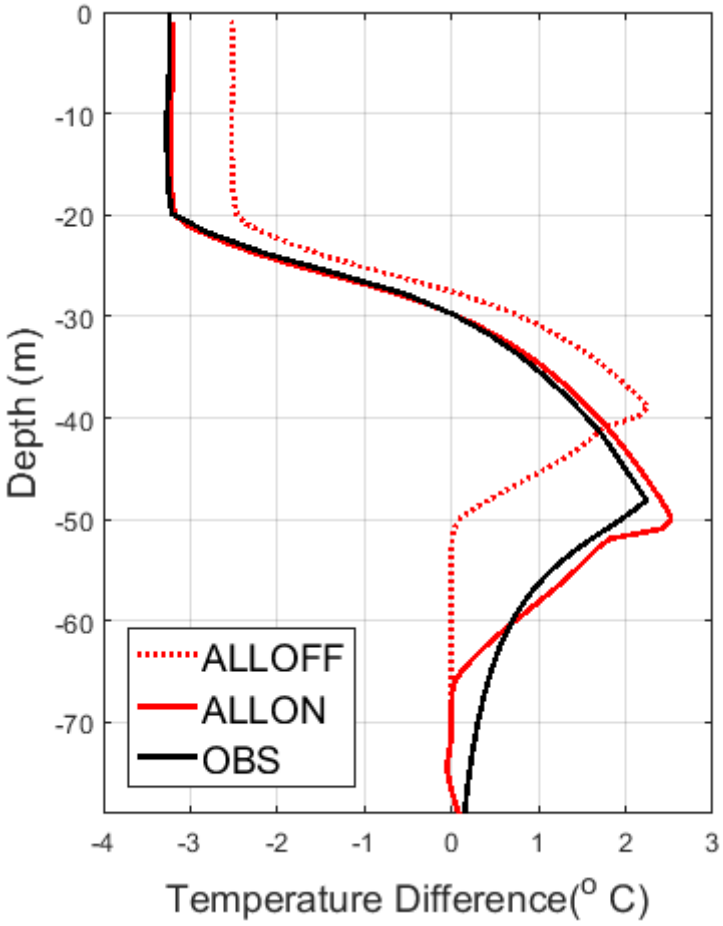

Figure 4.9: Vertical profiles of observed and simulated storm-induced temperature changes associated with Hurricane Felix in August 1995.

To quantify the wave effects on the accumulative effect of the upper ocean temperature change, we calculate the depth-integrated heat anomaly (DIH), which is used to illustrate the heat flux of the upper ocean. The simulation with all the wave effects (Exp-Allon) increases the mixed layer heat loss (0-29 m) by ~30% more than that of Exp-Alloff and reaches 336.3 MJ/m^2 which agrees well with the measurement results. The heat gained below the surface OML (29- 70 m) increases by almost 40% with the inclusion of wave effects, but still underestimates the observed heat gain below the surface OML. This underestimation may be explained by not including the three dimensional processes, especially near the base of seasonal thermocline (55m-70m).

Table 4.3: Depth integrated heat anomaly of observations and simulations for the depth intervals of 0-29 m ($DIH_{0\text{-}29}$), 29-70 m ($DIH_{29\text{-}70}$), and 0-70 m ($DIH_{0\text{-}70}$).

DIH (MJ/m^2)	ALLOFF	ALLON	OBS
0-29 m	-256.3	-336.3	-337.9
29-70 m	122.3	192.3	222.8
0-70 m	-144.0	-144.0	-115.1

4.3.2 Simulated Dynamical Responses

Time series of simulated and observed currents at depths of 25 m and 44 m are shown in Figure 4.11. The dominant frequency for simulated currents (both with and without surface wave effects) is estimated to be 0.0446 cph (or dominant periods of 22.4 hours) based on the rotary spectra analysis, which is 1.7% higher than the local inertial

frequency. Thus, the frequency-shifted phenomenon exists in the simulated currents, though the simulated frequency shifts less than that of BTM observations (0.0469 cph, or near-inertial periods of 21.3 hours). Similar to the observations, the u and v components are out of phase by $\pi/2$ with v as the leading component in all eight model experiments, which indicates that wave effects do not modify the phases of ocean currents.

As discussed above, the incorporation of surface gravity wave effects does not significantly modify the phase and frequency of the NIC, but it does have remarkable impacts on amplitudes of the NIC. The band-pass filter is applied to extract the near-inertial amplitudes of both simulations and BTM observations (Figure 4.10). At 25 m, the simulated amplitudes with surface wave effects (Exp-Allon) reach 70 cm/s in maximum, gradually decays with the e-folding time scale of ~16 days, and slightly increases on August 20 due to a high-wind event, which agrees well with the observations. By comparison, the near-inertial amplitudes simulated without wave effects (Exp-Alloff) are underestimated by ~30% of the observations.

At 44 m, the simulation with wave effects (Exp-Allon) performs comparatively well in the first three days of the hurricane's forcing, with the maximum amplitude up to ~67 cm/s. The response of inertial currents in the mixed layer is nearly instantaneous and vertically uniform with only a few hours delay at the mixed layer base [e.g., Qi et al. 1995]. The discrepancy occurs since August 19. Since then, observed near-inertial amplitudes decay faster than those of the 'waves' simulation (Exp-Allon). This discrepancy in the decay rates is understandable, since the depth of 44 m is near the base of the mixed layer where vigorous decaying processes occur. These processes include

enhanced turbulent shear instabilities at the mixed layer-thermocline interface [e.g., Herert and Moum, 1994], energy radiation by internal gravity waves [e.g., D'Asaro et al., 1995], and energy transfer from near-inertial waves to higher frequency internal waves [e.g., Henyey et al., 1986], etc. However, processes, such as the latter two, are not incorporated in our 1D GOTM model. Though the decay rate of the NIC is underestimated at the depth of 44 m by Exp-allon, the simulation of amplitude magnitude is significantly improved with the including of wave effects. Without wave effects, simulated near-inertial amplitudes are only one third of the observation. This remarkable underestimation is likely induced by the underestimation of the mixed layer depth in Exp-Alloff which is only 36 m, 10 m shallower than that of Exp-Allon.

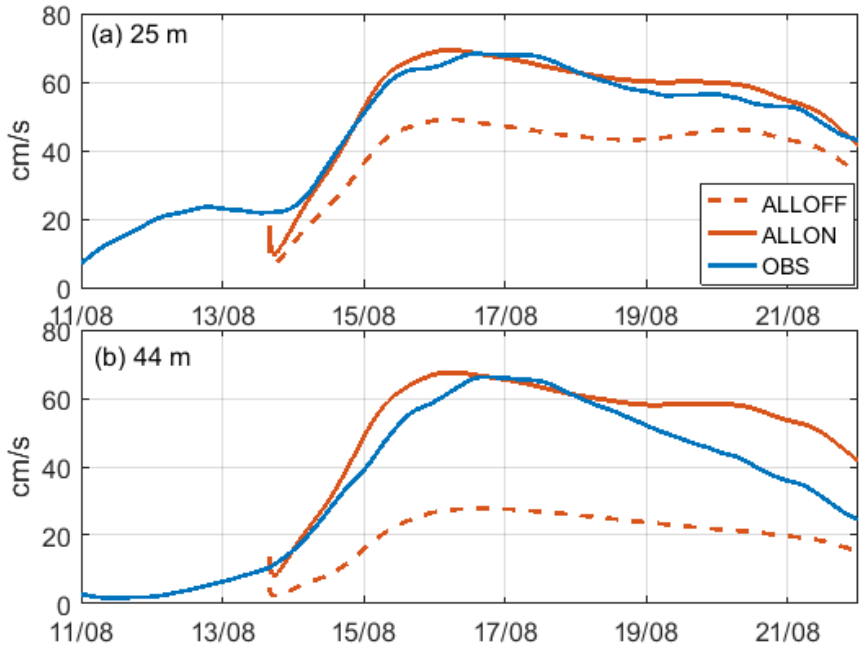

Figure 4.10: Time series of observed (blue curves) band-pass filtered inertial current amplitude (cm/s) in comparison to GOTM simulations (red curves) of Exp-Allon (solid) and Exp-Alloff (dashed) at depths of 25 m (upper panel), and 44 m (lower panel).

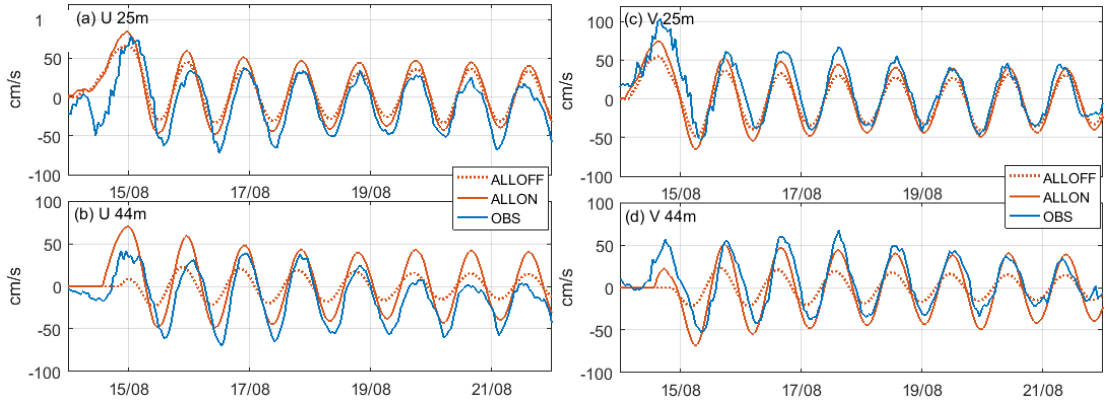

Figure 4.11: (a-b)Time series of observed (blue curves) eastward current (cm/s) in comparison to GOTM simulations (red curves) of Exp-allon (solid) and Exp-alloff (dashed) at depths of 25 m (upper panel), and 44 m (lower panel). (c-d) Same as Figure 4.10ab, but for northward current component.

Chapter 5
Summary and Discussion

The improvement of storm intensity prediction requires a better understanding of upper ocean responses to storms. In this thesis, the surface gravity wave effects on the upper ocean thermal and dynamic responses to fast-moving storms were investigated, and the dominant wave-related processes were quantified. A one-dimensional depth-dependent general ocean turbulence model (GOTM) was modified by incorporating wave-related processes. Major wave-related processes, surface wave breaking (WB), Langmuir circulation (LC) and Coriolis Stokes force (CSF), were considered in this modified GOTM with the wave age effects. This modified GOTM was used to simulate the upper ocean responses to hurricanes: (a) Hurricane Arthur (2014) over the coastal ocean over the Scotian Shelf (Section 3); and (b) Hurricane Felix (1995) over the open ocean near Bermuda in the northwest Atlantic (Section 4). The high-resolution glider measurements made during Hurricane Arthur and the Bermuda Testbed Mooring measurements made during Hurricane Felix were used to assess the model simulations and investigate the ocean responses to storms particularly with surface wave effects. The major conclusions for these studies are summarized as follows.

5.1 Summary of Results

The surface gravity wave effects were shown to have significant impact on the upper ocean responses to storms in terms of both thermal responses and dynamical responses. The wave effects can modify significantly the storm-induced temperature changes of the upper ocean, especially intensifying the cooling in the OML and heating the water below the OML at the early forced stage. This leads to an improvement of GOTM simulations by reducing the underestimation of both the storm-induced upper ocean cooling and the OML deepening. The wave effects modify the thermal responses mainly by enhancing the upper ocean turbulent intensities, illustrated by the intensified turbulent kinetic energy of the upper ocean. By including wave effects, the simulated hydrographic fields in the OML were found to be more homogeneous than those without wave effects. This can cause stronger current shears near the base of the OML, which induces more cold water entering the OML from the thermocline. Subsequently, the major thermal responses of the upper ocean cooling and heating below the OML were intensified by the surface wave effects. In addition, wave effects also contribute to the simulation responding more rapidly to storm forcing.

For the dynamic responses, this thesis focused on the surface gravity wave effects on the storm-induced near-inertial current responses. Wave effects can modify significantly the simulated near-inertial amplitudes but have very limited impact on the phases and dominant frequencies of the NICs. Wave effects on the NIC amplitudes were illustrated by the larger simulated NIC amplitudes near the base of the OML in Exp-Allon compared

to Exp-Alloff. Due to the simulated more homogeneous OML in Exp-Allon than Exp-Alloff, the simulated decay rate of the NIC amplitudes in the vertical direction were decreased in Exp-Allon. Assessed by the observations made during Hurricane Felix, the simulated NIC amplitudes in Exp-Allon showed better agreements with observations, with the NIC amplitudes in Exp-Allon to be two times larger than those of Exp-Alloff near the base of the OML. The wave effects also made the near-inertial energy to transport more efficiently to deeper layers. The same phase and dominant frequency were obtained by both simulations with and without wave effects, and the blue shift of the dominant frequency can always be detected.

Numerical process studies were conducted to examine the contribution of each wave-related process in the upper ocean response to storms at the storm forcing stage, during which wave effects play a more important role than during other stages due to their fast responding characteristics. The effects of wave breaking and Langmuir circulation were found to play essential roles and the contributions made by CSF effects were minor at the forcing stage. It should be noted that the surface wave breaking was parameterized as both a source of the TKE flux at the surface [Craig and Banner, 1994] and the momentum flux [He and Chen, 2011]. The WB-induced momentum flux with the wave-age-dependent vertical distribution was found to be more efficiently in modifying the storm-induced ocean thermal responses compared to the WB-induced TKE flux. The influence of WB-induced TKE flux was found to be confined at the surface. The wave-age-dependent momentum distribution was of importance for the young-wave sea state, which exhibited a minimum vertical decay rate at the wave age of 16 [Cai et al, 2017].

5.2 Future work

In this thesis, we investigated surface wave effects on the upper ocean responses to storms using a modified 1D depth-dependent GOTM model and conducted case studies of Hurricane Arthur and Hurricane Felix. Although we argued that the upper ocean responses to these two fast-moving storms were dominated by 1D processes, there are limitations to use the 1D depth-dependent model. For instance, processes, such as the storm-induced upwelling and advection may also play a role in the upper ocean responses to storms, but are not simulated by the 1D circulation model. A future research direction is to include wave effects in three-dimensional ocean circulation models such as ROMS (Regional Ocean Modelling System) or NEMO (Nucleus for European Modelling of the Ocean). In this case, the 3D models with surface gravity wave effects can be applied to slowly-moving storms which have more coupling with the ocean. Wave effects on storm-induced ocean responses during the relaxation stage when the ocean tends to recover from the storm influence can also be examined. We can also investigate the different contributions made by wave effects during forcing and relaxation stages, or in different cases of storms with various translation speeds. In addition, the wave effects on the asymmetric structures of storms can also be investigated.

Besides these studies of the physical processes, the performances of GOCMs are expected to be improved with the inclusion of surface wave effects, as well as the skill of the atmosphere-ocean coupled models, especially in extreme weather events. Based on the IPCC assessment report [IPCC, 2014], in the future, a likely increase in the numbers

of the most intense storms and a decrease in relatively weak storms as projected by embedded high-resolution models and global models are demonstrated. But the confidence in these results is low. The incorporation of surface wave effects in GOCMs is expected to improve the projection confidence for the future extreme weather events.

In this thesis, the k-ϵ turbulent scheme was applied. This two-equation turbulent scheme may be expected to have good representations of turbulent processes but may also be time-consuming in three-dimensional circulations models, particularly with high resolutions. Studies of surface waves effects on the upper ocean responses have been done used different turbulent schemes, e.g., Reichl et al [2016] explicitly include the sea-state-dependent impacts of the Langmuir circulation based on the KPP bulk closure. For future studies, a variety of turbulent schemes such as Price-Weller-Pinkel (PWP), K Profile Parameterization (KPP), and Mellor-Yamada 2.5 (MY) may be applied in model simulations. In the future study, we can also investigate the performances of different turbulent schemes and the sensitivity of model simulations on using different turbulent schemes.

The Stokes drift profiles are important to the wave effects parameterization, since both the CSF and LC effects are sensitive to these profiles. In this thesis, the profiles of Stokes drift were parameterized following the approach suggested by Breivik et al. [2004]. In the future, the Stokes drift profiles produced by wave models (e.g., SWAN or WW3) will be applied in model simulations. The sensitivity experiments will be conducted to detect the sensitivity on using different Stokes profiles. There are also other variables, e.g., the

surface wave-breaking induced energy flux, which will be replaced with wave model outputs and expected to better represent the realistic ocean conditions.

Bibliography

Agrawal, Y.C., Terray, E.A., Donelan, M.A., Hwang, P.A., Williams, A.J., Drennan, W.M., Kahma, K.K. and Krtaigorodskii, S.A., 1992. Enhanced dissipation of kinetic energy beneath surface waves. Nature, 359(6392), 219-220.

Ardhuin, F. and Jenkins, A.D., 2006. On the interaction of surface waves and upper ocean turbulence. Journal of physical oceanography, 36(3), 551-557.

Axell L.B., 2002. Wind-driven internal waves and langmuir circulations in a numerical ocean model of the southern Baltic sea. Journal of Geophysical Research: Oceans, 107(C11), 3204, doi: 10.1029/2001JC000922.

Babanin, A., 2011. Breaking and dissipation of ocean surface waves. Cambridge University Press, 480.

Belcher, S.E., Grant, A.L., Hanley, K.E., Fox-Kemper, B., Van Roekel, L., Sullivan, P.P., Large, W.G., Brown, A., Hines, A., Calvert, D. and Rutgersson, A., 2012. A global perspective on Langmuir turbulence in the ocean surface boundary layer. Geophysical Research Letters, 39, L18605, doi:10.1029/2012GL 052932.

Bender, M.A., Ginis, I. and Kurihara, Y., 1993. Numerical simulations of tropical cyclone-ocean interaction with a high-resolution coupled model. Journal of Geophysical Research: Atmospheres, 98(D12), 23245-23263.

Bender, M.A., Ginis, I., Tuleya, R., Thomas, B. and Marchok, T., 2007. The operational GFDL coupled hurricane-ocean prediction system and a summary of its performance. Monthly Weather Review, 135(12), 3965-3989.

Black, P.G., 1983. Ocean temperature changes induced by tropical cyclones. Ph.D. dissertation, The Pennsylvania State University, 278 pp.

Black, P.G., D'Asaro, E.A., Sanford, T.B., Drennan, W.M., Zhang, J.A., French, J.R., Niiler, P.P., Terrill, E.J. and Walsh, E.J., 2007. Air–sea exchange in hurricanes: synthesis of observations from the coupled boundary layer air–sea transfer experiment. Bulletin of the American Meteorological Society, 88(3), 357-374.

Brainerd, K.E. and Gregg, M.C., 1995. Surface mixed and mixing layer depths. Deep Sea Research Part I: Oceanographic Research Papers, 42(9), 1521-1543.

Breivik, Ø., Janssen, P.A. and Bidlot, J.R., 2014. Approximate stokes drift profiles in deep water. Journal of Physical Oceanography, 44(9), 2433-2445.

Burchard, H. and Baumert, H., 1995. On the performance of a mixed-layer model based on the κ-ε turbulence closure. Journal of Geophysical Research: Oceans, 100(C5), 8523-8540.

Burchard, H., Petersen, O. and Rippeth, T.P., 1998. Comparing the performance of the Mellor-Yamada and the κ-ε two-equation turbulence models. Journal of Geophysical Research: Oceans, 103(C5), 10543-10554.

Burchard, H., Bolding, K., Villarreal, M.R., 1999. GOTM -- a general ocean turbulence model. Theory, applications and test cases. Technical Report EUR 18745 EN, European Commission.

Chang, S.W., 1985. Deep ocean response to hurricanes as revealed by an ocean model with free surface. Part I: Axisymmetric case. Journal of physical oceanography, 15(12), 1847-1858.

Chen, S.S., Zhao, W., Donelan, M.A., and Tolman, H.L., 2013. Directional wind-wave coupling in fully coupled atmosphere-wave-ocean models: Results from CBLAST-Hurricane. Journal of the Atmospheric Sciences, 70(10), 3198-3215.

Cione, J.J. and Uhlhorn, E.W., 2003. Sea surface temperature variability in hurricanes: Implications with respect to intensity change. Monthly Weather Review, 131(8), 1783–1796.

Craig, P.D. and Banner, M.L., 1994. Modeling wave-enhanced turbulence in the ocean surface layer. Journal of Physical Oceanography, 24(12), 2546-2559.

Craik, A.D. and Leibovich, S., 1976. A rational model for Langmuir circulations. Journal of Fluid Mechanics, 73(3), 401-426.

D'Asaro, E.A., 2003. The ocean boundary layer below Hurricane Dennis. Journal of Physical Oceanography, 33(3), 561-579.

D'Asaro, E.A., Thomson, J., Shcherbina, A.Y., Harcourt, R.R., Cronin, M.F., Hemer, M.A. and Fox-Kemper, B., 2014. Quantifying upper ocean turbulence driven by surface waves. Geophysical Research Letters, 41(1), 102-107.

Dickey, T., Frye, D., McNeil, J., Manov, D., Nelson, N., Sigurdson, D., Jannasch, H., Siegel, D., Michaels, T. and Johnson, R., 1998. Upper-ocean temperature response to Hurricane Hurricane Felix as measured by the Bermuda Testbed Mooring. Monthly Weather Review, 126(5), 1195-1201.

Dickey, T., Zedler, S., Yu, X., Doney, S.C., Frye, D., Jannasch, H., Manov, D., Sigurdson, D., McNeil, J.D., Dobeck, L. and Gilboy, T., 2001. Physical and biogeochemical variability from hours to years at the Bermuda Testbed Mooring site: June 1994-March 1998. Deep Sea Research Part II: Topical Studies in Oceanography, 48(8), 2105-2140.

Domingues, R., Goni, G., Bringas, F., Lee, S.K., Kim, H.S., Halliwell, G., Dong, J., Morell, J. and Pomales, L., 2015. Upper ocean response to Hurricane Gonzalo (2014): Salinity effects revealed by targeted and sustained underwater glider observations. Geophysical Research Letters, 42(17), 7131-7138.

Emanuel, K.A., 1991. The theory of hurricanes. Annual Review of Fluid Mechanics, 23(1), 179-196.

Emanuel, K., 2001. Contribution of tropical cyclones to meridional heat transport by the oceans. Journal of Geophysical Research: Atmospheres, 106(D14), 14771-14781.

Emanuel, K, 2003. Tropical cyclones. Annual Review of Earth and Planetary Sciences, 31, 75-104.

Emanuel, K., DesAutels, C., Holloway, C. and Korty, R., 2004. Environmental control of tropical cyclone intensity. Journal of the atmospheric sciences, 61(7), 843-858.

Fairall, C.W., Bradley, E.F., Rogers, D.P., Edson, J.B. and Young, G.S., 1996. Bulk parameterization of air- sea fluxes for tropical ocean- global atmosphere coupled-ocean atmosphere response experiment. Journal of Geophysical Research: Oceans, 101(C2), 3747-3764.

Fan, Y. and Griffies, S.M., 2014. Impacts of parameterized Langmuir turbulence and nonbreaking wave mixing in global climate simulations. Journal of Climate, 27(12), 4752-4775.

Fisher, E.L., 1958. Hurricanes and the sea-surface temperature field. Journal of meteorology, 15(3), 328-333.

Gerbi, G.P., Trowbridge, J.H., Edson, J.B., Plueddemann, A.J., Terray, E.A. and Fredericks, J.J., 2008. Measurements of momentum and heat transfer across the air-sea interface. Journal of Physical Oceanography, 38(5), 1054-1072.

Gill, A.E., 1984. On the behavior of internal waves in the wakes of storms. Journal of Physical Oceanography, 14(7), 1129-1151.

Ginis, I., 1995. Ocean response to tropical cyclone. Chapter 5 of Global perspectives on tropical cyclones. WMO/TD-No. 693, 198-260.

Ginis, I., 2002. Tropical cyclone-ocean interactions. Advances in Fluid Mechanics, 33, 83-114.

Glenn, S.M., Miles, T.N., Seroka, G.N., Xu, Y., Forney, R.K., Yu, F., Roarty, H., Schofield, O. and Kohut, J., 2016. Stratified coastal ocean interactions with tropical cyclones. Nature communications, 7, 1-10, doi:10.1038/ncomms1088.

Hasselmann, K., 1970. Wave- driven inertial oscillations. Geophysical and Astrophysical Fluid Dynamics, 1(3-4), 463-502.

Hamlington, P.E., Van Roekel, L.P., Fox-Kemper, B., Julien, K. and Chini, G.P., 2014. Langmuir–submesoscale interactions: descriptive analysis of multiscale frontal spindown simulations. Journal of Physical Oceanography, 44(9), 2249-2272.

Harcourt, R.R. and D'Asaro, E.A., 2008. Large-eddy simulation of Langmuir turbulence in pure wind seas. Journal of Physical Oceanography, 38(7), 1542-1562.

He, H. and Chen, D., 2011. Effects of surface wave breaking on the oceanic boundary layer. Geophysical Research Letters, 38, L07604, doi:10.1029/2011GL046665.

Hebert, D., and Moum, J.N. (1994). Decay of a near-inertial wave. Journal of physical oceanography, 24(11), 2334-2351.

Hsu, S. A., Eric A. Meindl, and David B. Gilhousen, 1994. Determining the Power-Law Wind-Profile Exponent under Near-Neutral Stability Conditions at Sea, Applied Meteorology, 33(6), 757–765.

Huang, C.J., Qiao, F., Song, Z. and Ezer, T., 2011. Improving simulations of the upper ocean by inclusion of surface waves in the Mellor-Yamada turbulence scheme. Journal of Geophysical Research: Oceans, 116(C1), doi: 10.1029/2010JC006320.

IPCC, 2014. Climate Change 2014: Synthesis Report. Contribution of Working Groups I, II and III to the Fifth Assessment Report of the Intergovernmental Panel on Climate Change [Core Writing Team, R.K. Pachauri and L.A. Meyer (eds.)]. IPCC, Geneva, Switzerland, 151.

Jarosz, E., Mitchell, D.A., Wang, D.W., and Teague, W.J. (2007). Bottom-up determination of air-sea momentum exchange under a major tropical cyclone. Science, 315(5819), 1707-1709.

Johnston, T.M.S., Chaudhuri D., Mathur M., Rudnick D.L., Sengupta D., Simmons H.L., Tandon A., Venkatesan R., (2016). Decay mechanisms of near-inertial mixed layer oscillations in the Bay of Bengal. Oceanography, 29, 180-191.

Jordan, C.L. and Frank, N.L., 1964. On the influence of tropical cyclones on the sea surface temperature field. Proceedings Symposium Topical Meteorology, New Zealand Meteorol Service, 614-622.

Kantha, L.H. and Clayson, C.A., 2004. On the effect of surface gravity waves on mixing in the oceanic mixed layer. Ocean Modelling, 6(2), 101-124.

Kukulka, T., Plueddemann, A.J., Trowbridge, J.H. and Sullivan, P.P., 2010. Rapid mixed layer deepening by the combination of Langmuir and shear instabilities: A case study. Journal of Physical Oceanography, 40(11), 2381-2400.

Lai, D.Y. and Sanford, T.B., 1986. Observations of hurricane-generated, near-inertial slope modes. Journal of physical oceanography, 16(4), 657-666.

Lamb, P.J., 1984. On the mixed-layer climatology of the north and tropical Atlantic. Tellus. Series A, Dynamic meteorology and oceanography, 36(3), 292-305.

Large, W., and S. Pond, 1981: Open Ocean momentum flux measurements in moderate to strong winds. Journal of physical oceanography, 11, 324-336.

Large, W.G., McWilliams, J.C. and Niiler, P.P., 1986. Upper ocean thermal response to strong autumnal forcing of the northeast Pacific. Journal of Physical Oceanography, 16(9), 1524-1550.

Large, W.G., McWilliams, J.C. and Doney, S.C., 1994. Oceanic vertical mixing: A review and a model with a nonlocal boundary layer parameterization. Reviews of Geophysics, 32(4), 363-403.

Leaman, K.D. and Sanford, T.B., 1975. Vertical energy propagation of inertial waves: A vector spectral analysis of velocity profiles. Journal of Geophysical Research, 80(15), 1975-1978.

Leipper, D.F., 1967. Observed ocean conditions and Hurricane Hilda, 1964. Journal of the Atmospheric Sciences, 24(2), 182-186.

Leipper, D.F. and Volgenau, D., 1972. Hurricane heat potential of the Gulf of Mexico. Journal of Physical Oceanography, 2(3), 218-224.

Lemay, J., Helmuth, T., Craig, S.E., Burt, W.J., Fennel, K. and Greenan, B.J., 2018. Hurricane Arthur and its effect on the short-term variability of pCO_2 on the Scotian Shelf, NW Atlantic. Biogeosciences, 15(7), 2111.

Li, M., Zahariev, K. and Garrett, C., 1995. Role of Langmuir circulation in the deepening of the ocean surface mixed layer. Science, 270(5244), 1955-1957.

Li, M. and Garrett, C., 1997. Mixed layer deepening due to Langmuir circulation. Journal of Physical Oceanography, 27(1), 121-132.

Li, M., Garrett, C. and Skyllingstad, E., 2005. A regime diagram for classifying turbulent large eddies in the upper ocean. Deep Sea Research Part I: Oceanographic Research Papers, 52(2), 259-278.

Li, S., Song, J. and Fan, W., 2013. Effect of Langmuir circulation on upper ocean mixing in the South China Sea. Acta Oceanologica Sinica, 32(3), 28-33.

Lin, I.I., Wu, C.C., Emanuel, K.A., Lee, I.H., Wu, C.R. and Pun, I.F., 2005. The interaction of Supertyphoon Maemi (2003) with a warm ocean eddy. Monthly Weather Review, 133(9), 2635-2649.

Lin, I.I., Wu, C.C., Pun, I.F. and Ko, D.S., 2008. Upper-ocean thermal structure and the western North Pacific category 5 typhoons. Part I: Ocean features and the category 5 typhoons' intensification. Monthly Weather Review, 136(9), 3288-3306.

McWilliams, J.C., Sullivan, P.P. and Moeng, C.H., 1997. Langmuir turbulence in the ocean. Journal of Fluid Mechanics, 334, 1-30.

McWilliams, J.C., Huckle, E., Liang, J. and Sullivan, P.P., 2014. Langmuir turbulence in swell. Journal of Physical Oceanography, 44(3), 870-890.

Mellor, G.L. and Yamada, T., 1982. Development of a turbulence closure model for geophysical fluid problems. Reviews of Geophysics, 20(4), 851-875.

Mellor, G. L., 2001. One-dimensional, ocean surface layer modeling: a problem and a solution. Journal of Physical Oceanography, 31(3), 790-809.

Melville, W.K., Veron, F. and White, C.J., 2002. The velocity field under breaking waves: coherent structures and turbulence. Journal of Fluid Mechanics, 454, 203-233.

Michaels, A.F. and Knap, A.H., 1996. Overview of the US JGOFS Bermuda Atlantic Time-series Study and the Hydrostation S program. Deep Sea Research Part II: Topical Studies in Oceanography, 43(2), 157-198.

Moriasi, D. N., Arnold, J. G., Van Liew, M. W., Bingner, R. L., Harmel, R. D., & Veith, T. L. (2007). Model evaluation guidelines for systematic quantification of accuracy in watershed simulations. Transactions of the ASABE, 50(3), 885-900.

Moum, J.N. and Smyth, W.D., 2001. Upper ocean mixing processes. Encyclopedia of Ocean Sciences, 6, 3093-3100.

Nelson, N.B., 1996. Cover the Wake of Hurricane Felix. International Journal of Remote Sensing, 17(15), 2893-2895.

Noh, Y. and Jin Kim, H., 1999. Simulations of temperature and turbulence structure of the oceanic boundary layer with the improved near-surface process. Journal of Geophysical Research: Oceans, 104(C7), 15621-15634.

Noh, Y., Min, H.S. and Raasch, S., 2004. Large eddy simulation of the ocean mixed layer: The effects of wave breaking and Langmuir circulation. Journal of physical oceanography, 34(4), 720-735.

O'Brien, J.J. and Pillsbury, R.D., 1974. Rotary wind spectra in a sea breeze regime. Journal of Applied Meteorology, 13(7), 820-825.

Oey, L.Y., Ezer, T., Wang, D.P., Fan, S.J. and Yin, X.Q., 2006. Loop current warming by Hurricane Wilma. Geophysical Research Letters, 33(8), doi:10.1029/2006GL025873.

Ooyama, K., 1969. Numerical simulation of the life cycle of tropical cyclones. Journal of the Atmospheric Sciences, 26(1), 3-40.

Pasquero, C. and Emanuel, K., 2008. Tropical cyclones and transient upper-ocean warming. Journal of Climate, 21(1), 149-162.

Perlroth, I., 1969. Effects of oceanographic media on equatorial Atlantic hurricanes. Tellus, 21(2), 231-244.

Polton, J.A., Lewis, D.M. and Belcher, S.E., 2005. The role of wave-induced Coriolis–Stokes forcing on the wind-driven mixed layer. Journal of Physical Oceanography, 35(4), 444-457.

Polton, J.A. and Belcher, S.E., 2007. Langmuir turbulence and deeply penetrating jets in an unstratified mixed layer. Journal of Geophysical Research: Oceans, 112(C9), doi:10.1029/2007JC004205.

Powell, M.D., Vickery, P.J. and Reinhold, T.A., 2003. Reduced drag coefficient for high wind speeds in tropical cyclones. Nature, 422(6929), 279-283.

Price, J.F., 1981. Upper ocean response to a hurricane. Journal of Physical Oceanography, 11(2), 153-175.

Price, J.F., 1983. Internal wave wake of a moving storm. Part I. Scales, energy budget and observations. Journal of Physical Oceanography, 13(6), 949-965.

Price, J.F., Weller, R.A. and Pinkel, R., 1986. Diurnal cycling: Observations and models of the upper ocean response to diurnal heating, cooling, and wind mixing. Journal of Geophysical Research: Oceans, 91(C7), 8411-8427.

Price, J.F., Sanford, T.B. and Forristall, G.Z., 1994. Forced stage response to a moving hurricane. Journal of Physical Oceanography, 24(2), 233-260.

Qiao, F., Yuan, Y., Yang, Y., Zheng, Q., Xia, C. and Ma, J., 2004. Wave-induced mixing in the upper ocean: Distribution and application to a global ocean circulation model. Geophysical Research Letters, 31(11), doi:10.1029/2004GL019824.

Rapp, R.J. and Melville, W.K., 1990. Laboratory measurements of deep-water breaking waves. Philosophical Transactions of the Royal Society of London A: Mathematical, Physical and Engineering Sciences, 331(1622), 735-800.

Rascle, N. and Ardhuin, F., 2013. A global wave parameter database for geophysical applications. Part 2: Model validation with improved source term parameterization. Ocean Modelling, 70, 174-188.

Reichl, B.G., Wang, D., Hara, T., Ginis, I. and Kukulka, T., 2016. Langmuir turbulence parameterization in tropical cyclone conditions. Journal of Physical Oceanography, 46(3), 863-886.

Rodi, W., 1987. Examples of calculation methods for flow and mixing in stratified fluids. Journal of Geophysical Research: Oceans, 92(C5), 5305-5328.

Ruiz, S., Renault, L., Garau, B. and Tintore, J., 2012. Underwater glider observations and modeling of an abrupt mixing event in the upper ocean. Geophysical Research Letters, 39, L01603, doi: 10.1029/2011GL050078.

Sanford, T.B., Price, J.F. and Girton, J.B., 2011. Upper-ocean response to Hurricane Frances (2004) observed by profiling EM-APEX floats. Journal of Physical Oceanography, 41(6), 1041-1056.

Schade, L.R. and Emanuel, K.A., 1999. The ocean's effect on the intensity of tropical cyclones: Results from a simple coupled atmosphere-ocean model. Journal of the Atmospheric Sciences, 56(4), 642-651.

Shan, S., 2016. Eulerian and Lagrangian Studies of Circulation on the Scotian Shelf and Adjacent Deep Waters of the North Atlantic with Biological Implications. Ph.D. dissertation, Dalhousie University, p. 203.

Shay, L.K., Black, P.G., Mariano, A.J., Hawkins, J.D. and Elsberry, R.L., 1992. Upper ocean response to Hurricane Gilbert. Journal of Geophysical Research: Oceans, 97(C12), 20227-20248.

Shay, L.K., Mariano, A.J., Jacob, S.D. and Ryan, E.H., 1998. Mean and near-inertial ocean current response to Hurricane Gilbert. Journal of Physical Oceanography, 28(5), 858-889.

Shay, L.K., Goni, G.J. and Black, P.G., 2000. Effects of a warm oceanic feature on Hurricane Opal. Monthly Weather Review, 128(5), 1366-1383.

Sheng, J., Zhai, X., and Greatbatch, J.R., 2006. Numerical study of the storm-induced circulation on the Scotian Shelf during Hurricane Juan using a nested-grid ocean model. Progress in Oceanography, 70, 233-254.

Skyllingstad, E.D. and Denbo, D.W., 1995. An ocean large-eddy simulation of Langmuir circulations and convection in the surface mixed layer. Journal of Geophysical Research: Oceans, 100(C5), 8501-8522.

Smith, W.H.F., and Sandwell, D.T., 1997. Global seafloor topography from satellite altimetry and ship depth soundings. Science, 277, 1957-1962.

Steinberg, D.K., Carlson, C.A., Bates, N.R., Johnson, R.J., Michaels, A.F. and Knap, A.H., 2001. Overview of the US JGOFS Bermuda Atlantic Time-series Study (BATS): a decade-scale look at ocean biology and biogeochemistry. Deep Sea Research Part II: Topical Studies in Oceanography, 48(8), 1405-1447.

Stoney, L., Walsh, K., Babanin, A.V., Ghantous, M., Govekar, P. and Young, I., 2017. Simulated ocean response to tropical cyclones: The effect of a novel parameterization of mixing from unbroken surface waves. Journal of Advances in Modeling Earth Systems, 9(2), 759-780.

Sullivan, P.P., McWILLIAMS, J.C. and Melville, W.K., 2004. The oceanic boundary layer driven by wave breaking with stochastic variability. Part 1. Direct numerical simulations. Journal of Fluid Mechanics, 507, 143-174.

Sullivan, P.P., McWILLIAMS, J.C. and Melville, W.K., 2007. Surface gravity wave effects in the oceanic boundary layer: Large-eddy simulation with vortex force and stochastic breakers. Journal of Fluid Mechanics, 593, 405-452.

Sullivan, P.P. and McWilliams, J.C., 2010. Dynamics of winds and currents coupled to surface waves. Annual Review of Fluid Mechanics, 42, 19–42.

Sykulski, A.M., Olhede, S.C., Lilly, J.M. and Early, J.J., 2017. Frequency-Domain Stochastic Modeling of Stationary Bivariate or Complex-Valued Signals. IEEE Transactions on Signal Processing, 65(12), 3136-3151.

Teixeira, M.A.C. and Belcher, S.E., 2002. On the distortion of turbulence by a progressive surface wave. Journal of Fluid Mechanics, 458, 229-267.

Trenberth, K.E. and Fasullo, J., 2007. Water and energy budgets of hurricanes and implications for climate change. Journal of Geophysical Research: Atmospheres, 112(D23), doi:10.1029/2006JD008304.

Vincent, E.M., Madec, G., Lengaigne, M., Vialard, J. and Koch-Larrouy, A., 2013. Influence of tropical cyclones on sea surface temperature seasonal cycle and ocean heat transport. Climate dynamics, 41(7-8), 2019-2038.

Wagner, R.G., 1996. Decadal-scale trends in mechanisms controlling meridional sea surface temperature gradients in the tropical Atlantic. Journal of Geophysical Research: Oceans, 101(C7), 16683-16694.

Wang, P., and Sheng, J., 2016. A comparative study of wave-current interactions over the eastern Canadian shelf under severe weather conditions using a coupled wave-circulation model. Journal of Geophysical Research: Oceans, 121, 5252-5281.

Wright, R., 1969. Temperature structure across the Kuroshio before and after typhoon Shirley. Tellus, 21(3), 409-413.

Wu, L., Rutgersson, A. and Sahlée, E., 2015. Upper-ocean mixing due to surface gravity waves. Journal of Geophysical Research: Oceans, 120(12), 8210-8228.

Yablonsky, R.M. and Ginis, I., 2009. Limitation of one-dimensional ocean models for coupled hurricane-ocean model forecasts. Monthly Weather Review, 137(12), 4410-4419.

Zedler, S.E., Dickey, T.D., Doney, S.C., Price, J.F., Yu, X. and Mellor, G.L., 2002. Analyses and simulations of the upper ocean's response to Hurricane Felix at the Bermuda Testbed Mooring site: 13-23 August 1995. Journal of Geophysical Research: Oceans, 107(C12), doi:10.1029/2001JC000969.

Zijlema, M., Van Vledder, G.P. and Holthuijsen, L.H., 2012. Bottom friction and wind drag for wave models. Coastal Engineering, 65, 19-26.